High-resolution physicochemical dataset of atmospheric aerosols over the Tibetan Plateau and its surroundings

Jianzhong Xu[1,2*], Xinghua Zhang[2,a*], Wenhui Zhao[2,3,b], Lixiang Zhai[2,3,c], Miao Zhong[2,3], Jinsen Shi[4], Junying Sun[5], Yanmei Liu[2,d], Conghui Xie[2,e], Yulong Tan[2,3], Kemei Li[2,3], Xinlei Ge[6], Qi Zhang[7], Shichang Kang[2,3,8]

[1]School of Oceanography, Shanghai Jiao Tong University, Shanghai 200030, China.

[2]State Key Laboratory of Cryospheric Sciences, Northwest Institute of Eco-Environment and Resources, Chinese Academy of Sciences, Lanzhou 730000, China

[3]University of Chinese Academy of Sciences, Beijing 100049, China

[4]Key Laboratory for Semi-Arid Climate Change of the Ministry of Education, College of Atmospheric Sciences, Lanzhou University, Lanzhou 730000, China

[5]Key Laboratory of Atmospheric Chemistry of CMA, Chinese Academy of Meteorological Sciences, Beijing 100081, China

[6]Jiangsu Key Laboratory of Atmospheric Environment Monitoring and Pollution Control, Collaborative Innovation Center of Atmospheric Environment and Equipment Technology, School of Environmental Science and Engineering, Nanjing University of Information Science and Technology, Nanjing 210044, China

[7]Department of Environmental Toxicology, University of California, Davis, CA 95616, USA

[8]CAS Center for Excellence in Tibetan Plateau Earth Sciences, Beijing 100085, China

[a]now at: College of Urban and Environmental Sciences, Northwest University, Xi'an 710127, China.

[b]now at: Institute of Geochemistry, Chinese Academy of Sciences, Guangzhou 510640, China.

[c]now at: College of Resources and Environmental Sciences, Gansu Agricultural University, Lanzhou 730000, China.

[d]now at: College of Resources and Environment, Aba Teachers University, Wenchuan 623002, China.

[e]now at: State Key Joint Laboratory of Environmental Simulation and Pollution Control, College of Environmental Sciences and Engineering, Peking University, Beijing 100871, China.

Correspondence to: Jianzhong Xu (jzxu78@sjtu.edu.cn; jzxu@lzb.ac.cn) and Xinghua Zhang (zhangxinghua@lzb.ac.cn)

Abstract

Atmospheric aerosol in the Tibetan Plateau (TP) and its surroundings has attracted significant scientific interest in recent decades due to its notable impacts on regionally climatic and cryospheric changes, ecological and environmental securities, and the hydrological cycle. However, our understanding on the atmospheric aerosol in this remote region is highly limited by the scarcity of available dataset, owing to the extremely harsh natural conditions. This challenge has been mitigated in recent decades by establishing field observatories at typical sites within the TP and its surroundings. A continuous project initiated in 2015 aims to explore the properties and sources of atmospheric aerosols, as well as their regional differences, through multiple short-term intensive observations across this vast region utilizing a suite of high-time-resolution online instruments. This paper presents a systematic hourly scaled dataset of aerosol physicochemical and optical properties at eight sites across the TP and its surroundings derived from the project. It includes size-resolved chemical compositions of submicron aerosols, high-resolution mass spectra and sources of organic aerosols, size distributions of particle number concentrations, particle light scattering and absorption coefficients, particle light absorptions attributed to different carbonaceous substances including black carbon and brown carbon, and number concentrations of cloud condensation nuclei. In brief, atmospheric aerosols in these remote sites were all well-mixed and highly aged, reflecting their dominated regional transport sources. However, the southern TP region exhibited high contributions of carbonaceous organic aerosols, neutralized bulk submicron aerosols, and a relatively higher light absorption capacity, whereas in the northern TP region, secondary inorganic species were the main contributors to the overall acidic submicron aerosols. Beyond providing insights into the regional differences in aerosol sources and properties across the TP and its surroundings, the datasets will also benefit simulations of aerosol radiative forcing and evaluations of interactions among different Earth system components in numerical models in this region. The datasets are accessible through the National Cryosphere Desert Data Center, Chinese Academy of Sciences (https://doi.org/10.12072/ncdc.NIEER.db2200.2022; Xu, 2022).

1 Introduction

Tibetan Plateau (TP), with an average elevation exceeding 4,000 m above sea level (a.s.l.) and spanning a surface area of approximately 2.5 million square kilometers, stands as the highest plateau on the Earth. Its high-altitude mountain ranges, integral to one of the world's most crucial cryospheric regions, have earned the TP the monikers "roof of the world", "Third Pole", and "Asian Water Tower" (Qiu, 2008; Yao et al., 2019). The TP and its surroundings play a pivotal role in influencing the global and regional climate systems, hydrological cycles, and cryospheric changes through its vast and complex topography and its function as a significant heat source (Duan and Wu, 2005; Yao et al., 2012; Chen et al., 2021). In recent decades, a major concern has focusing on the significant climatic warming and the rapid changes in the cryosphere of this region (Kang et al., 2010), which exhibits a warming trend that exceeding that of the Northern Hemisphere (0.34 vs. 0.29 °C/decade) (You et al., 2021; Zhou and Zhang, 2021).

Atmospheric aerosols, as one of the most complex and critical components in the atmosphere, significantly influence climatic warming and cryospheric changes in the TP regions. They exert crucial direct and indirect effects on atmospheric energy budget and the albedos of snow and ice surfaces, impacting Earth's climate system (Xu et al., 2009; Kang et al., 2019b). Notably, light-absorbing carbonaceous aerosols (CAs) such as black carbon (BC) and brown carbon (BrC) directly absorb solar radiation, warming the atmosphere and contributing to positive forcing on Earth's energy budget (Ramanathan et al., 2007; Kopacz et al., 2011). For instance, Li et al. (2018) demonstrated that BC causes significantly greater albedo reduction (~46%) and instantaneous radiative forcing (7–64 W m^{-2}) on aged snow surfaces of a TP glacier than mineral dust. Moreover, aerosol particles over the TP significantly affect ice cloud properties and cloud development through their semi-direct effects (Liu et al., 2019). Given the vast and remote nature of the TP, coupled with its complex topography, meteorology, and harsh environment, *in-situ* observation of atmospheric aerosols poses substantial challenges. Consequently, numerical model simulations based on reanalysis data have emerged as a predominant and crucial method in recent decades. Notable studies include Lau et al. (2006), who assessed the impact of atmospheric aerosols on the Asian summer monsoon intensification using the NASA finite-volume general circulation model; Kopacz et al. (2011), who explored the origin and radiative forcing

of BC in the TP and Himalayas with the GEOS-Chem global chemical transport model; and Liu et al. (2015), who examined the transport of summer dust and anthropogenic aerosols using a three-dimensional aerosol transport–radiation model with satellite data inputs. Despite the significant insights gained from these simulations, *in-situ* observations of atmospheric aerosols in the TP are increasingly recognized as critical for evaluating and enhancing model accuracy in this remote area. The absence of *in-situ* aerosol data to refine models introduces considerable uncertainty into the results. Furthermore, while model simulations primarily focus on spatial distribution across broad regions, they often overlook temporal variations or the inherent evolution mechanisms at high temporal resolution, which in-situ observations could illuminate.

Recent advancements in observational techniques and instrumentation have enabled numerous *in-situ* measurement within the TP and its surroundings, aiming to delineate the physical, chemical, and optical properties of aerosols, along with their potential sources, transport pathways, and regional distributions. A detailed compilation of direct ambient aerosol measurements in the TP, employing a variety of observational methods and instruments, is presented in Table S1 in the supplementary material. Notably, off-line atmospheric filter sampling has emerged as a key in-situ aerosol collection method in the TP, favored for its low-cost and feasibility under the region's harsh conditions and logistical constraints. This method has effectively captured the composition, size, light absorption properties, sources, and variations of ambient aerosols, including diverse CAs components such as BC, BrC, organic carbon (OC), water-soluble OC (WSOC), humic-like substances (HULS), and polycyclic aromatic hydrocarbons (PAHs) in the remote TP region (Cao et al., 2009; Zhao et al., 2013; Xu et al., 2014a; Zhang et al., 2014; Cong et al., 2015; Wan et al., 2015; Xu et al., 2015; Kang et al., 2016; Li et al., 2016b; Xu et al., 2020). Furthermore, off-line filter sampling has been instrumental in mapping the regional aerosol distribution across the TP, facilitated by its simplicity and the ability to conduct simultaneous observations at multiple locations (Li et al., 2016a; Chen et al., 2019; Kang et al., 2022). Despite these advancements, off-line filter sampling studies in the TP's remote regions remain insufficient for current needs. The gathered data is generally fragmented and unsystematic, characterized by low temporal resolution, limited aerosol property parameters, and sparse data points. Typically, these studies have been localized to specific sites, utilizing single instruments with temporal resolutions ranging from days to weeks over brief periods. Such low temporal

resolution limits the accurate understanding of aerosols' temporal evolution and underlying mechanisms, especially during rapid, short-term events. Additionally, integrating and comparing data across different research groups is challenging due to variations in research focuses, measured parameters, sampling methodologies, laboratory filter processing, and data analysis techniques. Moreover, despite the relative ease of off-line sampling, extensive areas of the TP still lack such observational efforts. To date, comprehensive research focusing on multiple aerosol parameters through real-time online consecutive measurements (with high temporal resolutions from minute to hour scales) at multiple sites remains a rarity in the TP.

Research on atmospheric aerosols in China has achieved significant advancements over the past decade. The Aerodyne high-resolution time-of-flight aerosol mass spectrometer (HR-ToF-AMS) has become a widely used online instrument, enabling numerous studies to characterize the real-time, size-resolved chemical compositions and sources of submicron aerosols (Li et al., 2017; Zhou et al., 2020). However, its application in the TP has been limited, a situation attributed to the instrument's demanding operational requirements and the area's challenging observation conditions. Since 2015, our research group has initiated a continuous and systematic observation project, aiming to investigate the regional differences on aerosol sources and properties across the TP. This effort involves annual deployments of the HR-ToF-AMS alongside other high-resolution, real-time online instruments at various sites. Remarkably, our dataset represents the first and only collection that extensively covers a wide range of aerosol parameters (including physical, chemical, and optical properties and their diverse sources) across multiple geographic environments (e.g., urban, remote, high-altitude mountain, grassland, and subtropical forest) within the TP and its surroundings. This is achieved through real-time and high-time-resolution online observations, providing a comprehensive resource for understanding regional aerosol variations and serving as essential input for future aerosol radiative forcing simulations and Earth system interaction assessments. The structure of this paper is as follows: Sections 2 and 3 describe the observation sites, instrumental deployments, and data processing. Section 4 presents the high-time-resolution aerosol data, encompassing physical, chemical, and optical properties as well as source information. The limitations and the uniqueness of our dataset are discussed in Section 5.

2 Observation site descriptions

Between 2015 and 2022, intensive observations of atmospheric aerosol chemistry were carried out at eight sites across the TP and its surroundings. These sites comprise seven remote sites (QOMS, Motuo, NamCo, Ngari, Waliguan, LHG, and Bayanbulak) and one urban site (Lhasa), the latter serving as a contrast for comparative analysis. Figure 1 illustrates the geographical locations of these sites along with photographs during each observation. Table 1 details the specifics of each site including the sampling periods and the instruments deployed during each field campaign. The subsequent sections provide brief descriptions these sites, arranged geographically from the southern to the northern parts of the TP.

2.1 QOMS

The Qomolangma Station for Atmospheric and Environmental Observation and Research, Chinese Academy of Sciences (86.56ºE, 28.21ºN; 4276 m a.s.l.; abbreviated as QOMS in this study, with similar abbreviations for other sites hereafter), is situated in the Rongbuk valley basin on the northern slope of Mt. Everest. The climate in the northern slope of Mt. Everest has obvious seasonal variation, heavily influenced by the Indian monsoon system (Bonasoni et al., 2010; Cong et al., 2015). During the pre-monsoon season (typically March to May), dominant westerlies facilitates the long-range transport of atmospheric pollutants from South Asia, making QOMS an ideal high-altitude observatory on the south edge of the TP for examining transboundary pollutant transport into the plateau's interior. In the summer monsoon season (June−August), prevailing southerly winds bring warm and wet airflow from the Indian Ocean, leading to increased humidity and precipitation in the plateau.

2.2 Motuo

Motuo County, located in the lower reaches of the Yarlung Tsangpo River on the southern slopes of the eastern Himalayas and Gangrigab Mountains in the southeast edge of the TP. The county, sited halfway up a mountain, enjoys a subtropical humid climate characterized by relatively high temperatures and abundant rainfall. With a small population of ~15,000, Motuo County remains one of the TP's most pristine regions. The sampling site in Motuo (29.30°N, 95.32°E; 1305 m a.s.l.) was located atop a hill overlooking the Yarlung Tsangpo Grand Canyon. This vantage point makes it an ideal location for directly monitoring the transboundary transport of atmospheric pollutants and moisture from Southeast Asia and the Indian Ocean into the TP.

2.3 NamCo

The Nam Co Station for Multisphere Observation and Research, Chinese Academy of Sciences (NamCo; 90.95ºE, 30.77ºN; 4730 m a.s.l.) is a high-altitude observatory in the south-central part of the TP. Situated at the southeast shore of Nam Co Lake, the station is surrounded by a pristine and isolated area. The region experiences a typical semi-arid plateau monsoon climate, characterized by increased precipitation during the summer monsoon season. NamCo is a pivotal inland site within the TP, predominantly influenced by air masses from the south and west.

2.4 Ngari

The Ngari Station for Desert Environment Observation and Research, Chinese Academy of Science (Ngari; 79.70°E, 33.39°N; 4270 m a.s.l.) is located in the Rutog County within the Ngari Prefecture of the Tibet Autonomous Region, China. This area is at the southwestern edge of the TP and is characterized by its semi-arid climate, sparse vegetation, and intense solar radiation. As a key member of "high-cold region observation and research network for land surface processes & environment of China", the Ngari station plays a crucial role in monitoring climate, hydrological, atmospheric, and ecological environmental changes in the TP's western territories. Additionally, it contributes to understanding the interactions between the Indian monsoon system and the westerlies.

2.5 Waliguan

The Waliguan Baseline Observatory (Waliguan; 100.9ºE, 36.28ºN; 3816 m a.s.l.) is one of the twenty-nine baseline stations of Global Atmosphere Watch (GAW) under the World Meteorological Organization (WMO). Situated at the top of Mt. Waliguan, which rises approximately 600 m, the observatory is located in a pristine region with minimal human activity impact. Waliguan is represented as a key observatory on the northeastern edge of the TP, predominantly influenced by air masses from the northeast during the summer. This location is strategic for studying the transport and impact of air pollutants from industrial regions in northwestern China to the TP in this study.

2.6 LHG

The Qilian Observation and Research Station of Cryosphere and Ecologic Environment, Chinese Academy of Sciences (LHG; 39.50°N, 96.51°E; 4180 m a.s.l.), is located approximately 1km from the terminus of Laohugou Glacier No.12. This glacier is

among the largest mountain glacier in the northern slope of the western Qilian Mountains. LHG serves as another notable station in the northeastern TP, distinctly remote from human settlements. The climate in this region is predominantly arid and continental, influenced by the East-Asian monsoon in summer and the Westerlies in winter. A pronounced mountain-valley breeze during summer facilitates the upward transport of air masses from lower altitudes, making LHG an ideal site for background air mass sampling and for investigating the transport and potential impacts of air pollutants from surrounding areas.

2.7 Bayanbulak

The Bayanbulak National Basic Meteorological Station (Bayanbulak; 84.35° N, 42.83° E; 2454 m a.s.l.) is located in the Bayanbulak grassland, northwest of Hejing County in the Xinjiang Uygur Autonomous Region, China. Bayanbulak lies within an intermontane basin in the central Tianshan Mountains, surrounded by numerous snow mountains with altitudes more than 3000 m. The climate in Bayanbulak grassland is characterized by a typical temperate continental mountain climate, with an annual average precipitation ranging between 200 to 300 mm. Bayanbulak town experiences minimal human activities and traffic, maintaining its pristine environment.

2.8 Lhasa

Lhasa (29.65°N, 91.03°E; 3650 m a.s.l.) is the capital of the Tibet Autonomous Region, China, and located in the south-central part of the TP. The city lies in a broad river valley, surrounded by mountains that reach up to 5500 m, with the Lhasa River passing through the city from west to east. Our observation site is located in Binhe Park, adjacent to the Lhasa River. Notably, the Norbulingka scenic area, one of the main activity centers for local Tibetans celebrating their religious festivals such as the Sho Dun festival, is located ~1 km to the northwest of the sampling site. Moreover, the Potala Palace, the center of Tibetan Buddhism, is ~1.8 km to the northeast. Given Lhasa's unique energy structure and the distinct living habits of the residents, comparative observations are carried out at this urban site. These studies aim to investigate the primary aerosol properties and sources, particularly from various residential combustion activities.

3 Online sampling, instrumental setup, and data processing

3.1 Online real-time aerosol sampling over the TP

Atmospheric aerosol observations were conducted at each site using a suite of real-time, high-resolution instruments. This instruments typically included a HR-ToF-AMS (Aerodyne Research Inc., Billerica, MA, USA) to determine the chemical composition (organic aerosol (OA), nitrate, sulfate, ammonium, and chloride) of non-refractory submicron aerosol (PM_1); A scanning mobility particle sizer (SMPS, model 3936, TSI Inc., Shoreview, MN, USA) was used to measure the size distribution and number concentration of submicron particles; A photoacoustic extinctiometer (PAX, DMT Inc., Boulder, CO, USA) was used for obtaining particle light absorption, scattering, and extinction coefficients (Babs, Bscat, and Bext) along with single scattering albedo (SSA) at 405 nm, as well as BC mass concentration; An Aethalometer (model AE33/AE31, Magee Scientific Corp., Berkeley, CA, USA) was used for acquiring the B_{abs} across seven wavelengths (370−950 nm); A cloud condensation nuclei (CCN) counter (model CCN-100, DMT Inc., Boulder, CO, USA) measured CCN number concentrations at various water vapor supersaturations (SS). The measurement uncertainties for each instrument are difficult to quantify based on data from a single instrument. The uncertainty showing below are referred from other studies: <30% for HR-ToF-AMS (Jimenez et al., 2016) and SMPS, <40% for Aethalometer (Backman et al., 2017), <10% for PAX (Selimovic et al., 2018), and <25% for CCNC (Rose et al., 2008). Details on the specific instruments deployed and the sampling periods for each observation campaign are summarized in Table 1.

The HR-ToF-AMS was the cornerstone instrument for atmospheric aerosol chemistry observations across all field campaigns. The SMPS was deployed at QOMS, Motuo, LHG, and Lhasa, whereas the PAX was employed at QOMS, Motuo, Ngari, Waliguan, and Lhasa. The Aethalometer was utilized at QOMS, NamCo, and Waliguan, with the CCN-100 operational at Motuo, Waliguan, and LHG. Field observations in the southern, western, and central regions of the TP were predominantly conducted during the pre-monsoon season, aimed to study the transboundary transport of pollutants from South Asia into the TP, under the influence of Westerlies and the Indian monsoon. For instance, observations took place from 12 April to 12 May at QOMS, Motuo from 26 March to 22 May, NamCo from 31 May to 1 July, and Ngari from 1 Jun to 5 July. On the other hand, measurements in the remote regions of the northern TP and its surroundings were carried out during the summer to track aerosol transport from surrounding polluted areas, considering the effects of the Westerlies or the intensified East Asian monsoon.

Specifically, observations occurred from 1 to 31 July at Waliguan, from 4 to 29 August at LHG, and from 29 August to 26 September at Bayanbulak. The observation at Lhasa was conducted from 31 August to 26 September, focusing on capturing the peak atmospheric oxidation capacity during the summer.

3.2 Instrumental setup

Despite the variations in instrumentation across different observation campaigns, the core setup for sampling was largely consistent. Figure 1b illustrates the standard sampling configuration for each campaign typically involved housing all instruments within an air-conditioned trailer or room. The inlets were induced to the instruments from the roof with a cyclone (model URG-2000-30EH, URG Corp., Chapel Hill, NC, USA) in the front of the inlet to eliminate particles with an aerodynamic diameter (D_{va}) exceeding 2.5 μm. These fine particles were then passed through a Nafion dryer via 1/2-inch stainless steel tubing to dehumidify the airflows before being directed into the instruments for real-time analysis. For detailed information on the setup and methodology of the instruments, it can be found in our previous publications (Xu et al., 2018; Zhang et al., 2018; Zhang et al., 2019; Zhao et al., 2022).

3.3 Instrumental operation and data processing

The measurement principles, operation procedures, calibration methods, and data analysis for these instruments used in this study are thoroughly detailed in Texts S1−S4 of supplementary material. Here, we highlight only key descriptions and critical setting as follows: (1) The HR-ToF-AMS was operated at V-mode during most of the eight field campaigns to accommodate the relatively low signal-to-noise ratios due to low aerosol mass loading in the TP regions. (2) Particle size observations were not conducted during the NamCo and LHG campaigns due to a chopper malfunction in the HR-ToF-AMS. (3) Different relative ionization efficiency (RIE) values were used for ammonium and sulfate according to the ionization efficiency calibrations of HR-ToF-AMS in different campaigns. (4) Different size parameters were achieved according to the particle sizing calibrations in different campaigns. (5) Elemental ratios of OA such as oxygen-to-carbon (O/C), hydrogen-to-carbon (H/C), organic matter-to-organic carbon (OM/OC), and nitrogen-to-carbon (N/C), were determined using the improved method (Canagaratna et al., 2015). (6) A default collection efficiency (CE) value of 0.5 were employed to the HR-ToF-AMS measurements during the QOMS, NamCo, Ngari,

Waliguan, and Lhasa campaigns in consideration of their overall neutralized bulk submicron aerosols, whereas a composition-dependent CE (Middlebrook et al., 2012) value was adopted at Motuo, LHG, and Bayanbulak, where aerosols were slightly acidic. (7) Source apportionment of OA during all observations were performed by the positive matrix factorization (PMF) analysis. The details of the PMF solution determination for each site are not presented here but can be referenced in our previous publication for select campaigns (Xu et al., 2018; Zhang et al., 2018; 2019). (8) Only the chemical compositions of non-refractory PM_1 are reported for the Bayanbulak campaign due to the absence of BC observations. (9) The sample and sheath flow rates of SMPS were set at 0.3 and 3.0 L min^{-1}, respectively, at both QOMS and Lhasa, covering a particle size range between 14.6 and 661.2 nm in mobility diameter (D_m), whereas 0.5 and 5.0 L min^{-1} at LHG and Motuo sites with a range of 10.9−495.8 nm in D_m. (10) Aethalometer measurements were corrected for filter-based loading and multiple scattering effects. A traditional absorption Ångström exponents (AAE) method (Zhang et al., 2021) was adopted to apportion total B_{abs} into two parts of BC and BrC ($B_{abs,BC}$ and $B_{abs,BrC}$). (11) CCN number concentrations were measured at five different SS values of 0.2%, 0.4%, 0.6%, 0.8%, and 1.0% at a 30-min cycle during the Motuo, Waliguan, and LHG campaigns.

4 Aerosol properties, sources, and radiative forcing over the TP

4.1 Mass loading and chemical composition of submicron aerosols

Figure S1 presents the temporal variations of PM_1 chemical species (OA, nitrate, sulfate, ammonium, chloride, and BC) observed across the eight observations in the TP and its surroundings. The mass concentrations of PM_1 and its components exhibited distinct variations, with a few periods of high mass loading observed throughout each campaign's sampling period. Despite variations in sampling years (2015−2022), seasons (March−September), and altitudes (1350−4730 m a.s.l.) across these sites, the distinct PM_1 mass concentrations and chemical compositions clearly illustrate the regional difference among these sites. On average, total PM_1 mass concentrations across the eight campaigns ranged from 1.9 to 9.1 μg m^{-3} (Fig. 2 and Table 2). The highest mass concentration was observed at Waliguan, driven by the transport of anthropogenic aerosols and gaseous pollutants from urban centers in northwestern China. In contrast, the lowest values were observed at NamCo and Bayanbulak, reflecting their background and pristine environmental conditions. The average PM_1

mass level across the TP and its surroundings was comparable to those observed at other high-altitude, coastal, forest, and remote background sites globally (0.46−15.1 μg m^{-3}; Table 3), yet remains significantly lower than those observed at densely urban (34.4−71.5 μg m^{-3}) and suburban (21.4−44.9 μg m^{-3}) areas in other parts of China (Li et al., 2017). This suggests the predominantly clean atmospheric conditions in the remote and high-altitude regions of the TP.

The chemical compositions of PM_1 also exhibited significant regional differences across the TP (Fig. 2), highlighting varied aerosol sources in different areas of the TP. At five sites (QOMS, Motuo, NamCo, Ngari, and Lhasa) located in the southern, western, or central TP, OA and BC together accounted for as high as 64.9−85.7% of the total PM_1 mass (Table 2). This high contribution was largely attributed to the frequent transport of biomass-burning emissions from South and Southeast Asia to the TP during the pre-monsoon season (Bonasoni et al., 2010; Cong et al., 2015; Zhang et al., 2018), along with significant local biomass burning from religious activities in Lhasa (Cui et al., 2018; Zhao et al., 2022). In contrast, at the three northern sites (Waliguan, LHG, and Bayanbulak), inorganic species (sulfate, nitrate, and ammonium; referred to as SNA) accounted for more than 60% of the total PM_1. Sulfate was the most significant component of SNA (38.1−46.0%), aligning with observations from another high-altitude site in the northeastern TP (Menyuan; 28%) and various rural and remote sites (19–64%) in East Asia (Du et al., 2015). The pronounced SNA contributions, particularly sulfate, in the northern TP and its surroundings, were mainly related to the regional transport of anthropogenic aerosols and gaseous precursor from nearby urban areas as well as important in-cloud aqueous reactions during the transportation to the mountains (Zhang et al., 2019).

4.2 Bulk acidity, size distribution, and diurnal variation of submicron aerosols

Particle phase acidity significantly influences aerosol physicochemical properties, affecting hygroscopicity, toxicity, and heterogeneous reactions. The bulk acidity of submicron aerosols was evaluated at each site following the method in Zhang et al. (2007b) and Schueneman et al. (2021) using AMS measurements. A detailed description of this method can be found in Text S5 of the supplementary material or our previous publications (Zhang et al., 2018; Zhang et al., 2019). Notably, we observed clear regional variations between the southern and northern TP, largely due to differences in aerosol sources and composition (Fig. 3). Linear regression slopes at

QOMS, NamCo, Ngari, and Lhasa (located in the southern, western, or central TP) were fitted to be 1.2, 1.11, 0.98, and 1.18, respectively, indicating the submicron aerosols at these sites were generally neutralized, occasionally showing an excess of ammonium. The result is consistent with previous findings on high ammonia availability from agriculture emissions in the South Asia (Van Damme et al., 2015). Moreover, as reported in our previous publications, atmospheric aerosols at QOMS and NamCo were significantly influenced by biomass-burning emissions from South and Southeast Asia during the pre-monsoon season (Xu et al., 2018; Zhang et al., 2018), and Lhasa experienced intense biomass fuel burning during frequent religious festivals (Zhao et al., 2022). In contrast, submicron particles at the remaining four sites, particularly LHG and Bayanbulak in the north, were overall acidic, with regression slopes ranging from 0.73 to 0.86, where sulfate was a major PM_1 component (46.0% and 41.6%). Similar findings of acidic submicron aerosol particles have also been observed at Menyuan and LHG in the northern TP in previous studies (Du et al., 2015; Xu et al., 2015), mainly related to the transport of enriched SNA species or their gaseous precursors from the industrial areas in northwestern China.

The size distributions of non-refractory PM_1 chemical species, obtained from HR-ToF-AMS measurement, provide valuable insights into aerosol sources, oxidation degrees, mixing states, formation, transformation, and growth mechanisms as well as their impacts on CCN activity. Typically, size distributions for SNA species and oxidized OA peaked in the accumulation mode (~400−600 nm in D_{va}), as a result of secondary formation processes. In contrast, fresh organics from primary emission sources exhibit smaller size (Zhang et al., 2005b; Aiken et al., 2009). In this study, we focus on organics and the combined three SNA species to highlight regional variations in size distributions across the TP. As shown in Figs. 4a and S2 and Table 2, the peak diameters of OA and SNA size distributions varied significantly, from 584.4 and 634.5 nm at Ngari to a smaller size of 228.1 and 250.0 nm at Lhasa, respectively. This variation suggests the distinctly different sources and aging processes of atmospheric aerosols across the TP, particularly between those high-altitude remote sites and urban sites. For instance, bulk PM_1 at QOMS was reported to be internally well-mixed and aged, attributed to long-range transport from biomass-burning emissions in South Asia (Zhang et al., 2018), whereas local primary sources, including cooking, traffic exhausts, and biomass burning, totally accounted for more than 60% of the total OA in urban Lhasa (Zhao et

al., 2022). The crucial influence of aerosol sources on size distributions is further supported by the correlation between the mode size and O/C ratios of OA (R^2 = 0.74) (Fig. 4a).

The diurnal variations of PM_1 chemical compositions are typically influenced by multiple factors, including meteorological conditions (e.g., planetary boundary layer (PBL) height, wind direction and speed, temperature, relative humidity), various primary emission sources (e.g., vehicle exhausts during traffic rush hours, cooking emissions, and coal combustion emissions for heating), and distinct formation mechanisms (e.g., daytime photochemical oxidation, nighttime heterogeneous reactions, and gas-particle partitioning of secondary species). A comprehensive understanding of these diurnal variations is crucial for exploring the dynamic evolution of aerosol compositions and identifying the primary drivers (source, meteorology, or secondary formation) behind the variations in different chemical species.

Distinct diurnal patterns in the total PM_1 mass concentrations were observed across different field campaigns (Fig. 4b). At remote sites of QOMS, LHG, NamCo, and Waliguan, located in valleys or atop mountains, variations were largely governed by mountain-valley wind circulation and change in PBL height. For instance, QOMS exhibited a distinct diurnal pattern with continuously decreasing concentrations during the daytime, but relatively higher concentrations at night. The minimum occurred at around ~15:00 in this valley site, likely due to strong afternoon glacier winds and a higher PBL (Zhang et al., 2018). Conversely, LHG and NamCo experienced lower PM_1 concentrations from night to early morning, with increase in the afternoon, attributed at LHG to up-slope wind transport and at NamCo to aerosols descending from higher layers and enhanced afternoon transport from the west (Xu et al., 2018). A complex diurnal pattern of PM_1 was observed at Waliguan, influenced by diffusion conditions, wind directions, and air mass sources, including afternoon air masses from the northeast, which likely carried industrial pollutants (Zhang et al., 2019). At Motuo, the diurnal pattern of PM_1 was relatively stable, with two weak peaks linked to local combustion activities in the late morning and evening. Ngari exhibited relatively higher nighttime loadings and lower daytime loadings, mainly due to the variations of PBL height. Bayanbulak, on the other hand, had relatively low and stable PM_1 mass throughout the entire day due to its background location. In contrast, urban Lhasa displayed two pronounced peaks correlating with primary emissions during morning and evening rush

hours (Zhao et al., 2022). Although the diurnal pattern of PM_1 were mainly shaped by mountain-valley winds and PBL height in those remote sites, and primary emissions in the urban site in this study, secondary formation processes, including photochemical oxidation and aqueous-phase reactions were also played a key role in the formation of inorganic and organic aerosol species. This could be evidenced by the afternoon peaks of oxygenated OA (OOA) components observed across almost all the sites, which were commonly formed by photo-chemical processes (Xu et al., 2018; Zhang et al., 2018; Zhang et al., 2019; Zhao et al., 2022).

4.3 High-resolution mass spectrum and elemental ratios of organic aerosol

The high-resolution mass spectrum (HRMS) and elemental ratios of OA were determined to identify the possible sources, formation and evolution mechanisms, and oxidation states at each site. A direct comparison of the average O/C ratios from the eight field campaigns was presented in Fig. 5a. It is apparent that the O/C ratios at the remote sites of QOMS, Motuo, NamCo, Ngari, Waliguan, and LHG typically reached or exceeded 1.0, indicating highly oxidized OA. In contrast, Bayanbulak exhibited a lower O/C ratio of 0.69, and the urban site of Lhasa showed an even lower ratio of 0.44. These variations in O/C ratios across sites primarily reflect differences in OA sources and aging processes. Remote sites in the TP were generally received well-mixed and aged OA due to long-range transport (Xu et al., 2018; Zhang et al., 2018; Zhang et al., 2019). Meanwhile, local emissions from activities like cooking, traffic, and biomass burning significantly contribute to the OA in urban Lhasa, resulting in a comparatively low O/C ratio (Zhao et al., 2022). This pattern of higher O/C ratios at remote sites and lower ratios at urban sites were observed in previous findings across China, such as O/C ratios of 0.98, 1.11, and 1.16 observed at Mt. Wuzhi (Zhu et al., 2016), Mt. Yulong (Zheng et al., 2017), and LHG (Xu et al., 2015), respectively, versus urban sites where O/C ratios typically fell below 0.5 at most urban sites (Zhou et al., 2020). The Van Krevelen diagram, which plots H/C versus O/C ratios to illustrate changes in OA elemental composition due to atmospheric aging, shows an overall slope of −0.66 for the bulk OA across all campaigns. This result is comparable to slopes of −0.58 and −0.47 obtained in previous studies, further illustrating common pathways in OA aging (Chen et al., 2015; Zhou et al., 2020).

The average HRMSs of OA between the remote site (Waliguan) and the urban site (Lhasa) were directly compared to investigate the difference in ionic compositions (Fig.

5c). Waliguan was selected for comparison due to its representation of overall highly aged OA, a characteristic shared with other remote sites (Fig. S3). The HRMS of OA at Waliguan and Lhasa displayed significant differences. At Waliguan, the *m*/*z* 44, predominantly composed of CO_2^+ and a key marker for OOA, was the most prominent peak (18%) in the OA HRMS. The CO_2^+ and its related ions (CO^+, H_2O^+, HO^+ and O^+) together contributed over 41% of the total OA signals. Additionally, two oxygenated ion fragments ($C_xH_yO_1^+$ and $C_xH_yO_2^+$) accounted for as much as 66% of the total OA signals (Fig. 5c), suggesting the highly oxygenated nature of OA at this remote site. In contrast, the OA HRMS at Lhasa was remarkably similar to those observed in urban environments, with significant contributions from four *m*/*z* values at 43, 55, 57, and 60. These ions are recognized as markers for less oxidized OA or primary emissions related to traffic, cooking, and biomass burning (Zhang et al., 2005a; Alfarra et al., 2007; He et al., 2010), making up a significant contribution to the OA signals in Lhasa. Specifically, non-oxygenated ion fragments ($C_xH_y^+$) contributed as much as 64.5% of the total OA in Lhasa, whereas the oxygenated fragments accounted for only 33.6%. This pattern of fresh ion fragments in the OA HRMS in Lhasa is comparable to those measured at other urban cities, such as 56% and 59% in Lanzhou (Xu et al., 2014b; Xu et al., 2016), 51.2% in Nanjing (Wang et al., 2016), and 51.2% in New York (Sun et al., 2011).

4.4 OA components from PMF source apportionment

Source apportionments of OA were performed using PMF analysis on OA HRMS data for each field campaign. Figure 6 presents the average mass contributions of OA components from the selected 2−4 factor solutions across eight field campaigns, while Figure S4 details the specific HRMS signatures for each OA component. In regions with limited local emissions but significant influence from regional transport, such as NamCo, LHG, and Bayanbulak, two secondary OA factors with different oxidation degrees, namely a less oxidized OOA (LO-OOA) and a more oxidized OOA (MO-OOA), were identified. For instance, during the NamCo campaign, the MO-OOA and LO-OOA accounted for 59.0% and 41.0% of the total OA mass, with average O/C ratios of 0.96 and 0.49, respectively. The Bayanbulak campaign exhibited a similar result, with MO-OOA (average O/C of 1.12) and LO-OOA (average O/C of 0.55) accounting for 66.3% and 33.7% of the OA mass, respectively. Contrastingly, the LHG campaign revealed a different pattern, with 24.9% MO-OOA and 75.1% LO-OOA, albeit with

519 higher O/C ratios of 1.29 and 1.08, respectively. Note that the properties of each OOA
520 factor could be different across the locations in the TP despite the same name.
521 Additionally, biomass-burning-related OA (BBOA) was also a prevalent component in
522 the TP. At QOMS, the OA was composed by 42.4% MO-OOA, 43.9% BBOA, and 13.9%
523 nitrogen-containing OA (NOA), with average O/C ratios of 1.34, 0.85, and 1.10,
524 respectively. The high O/C ratio and significant contributions of BBOA and NOA at
525 QOMS were linked to biomass burning emissions transported from South Asia during
526 the pre-monsoon season (Cong et al., 2015; Zhang et al., 2018; Kang et al., 2019a). At
527 Waliguan, the OA was composed by 34.4% MO-OOA, 40.4% relatively aged BBOA
528 (agBBOA), 18.3% BBOA, and 6.9% hydrocarbon-like OA (HOA), with average O/C
529 ratios of 1.42, 1.02, 0.69, and 0.33, respectively. The agBBOA exhibited an enhanced
530 contribution to OA as the OA mass concentration increased, ranging from ~10% to 70%
531 when OA mass varied from <1.0 μg m^{-3} to 7 μg m^{-3} (Zhang et al., 2019). High
532 contributions of BBOA at Waliguan were associated with regional transport of biomass
533 burning emissions from areas in the northeast (Zhang et al., 2019). At Ngari, the OA
534 was composed by 43.7% MO-OOA, 28.5% LO-OOA, and 27.8% BBOA, with average
535 O/C ratios of 1.43, 1.00, and 0.56, respectively. In contrast, the Motuo exhibited OA
536 components of 36.9% MO-OOA, 46.9% LO-OOA, and 16.2% BBOA, with O/C ratios
537 of 1.30, 1.11, and 0.25, respectively. The lower BBOA contribution and O/C ratio at
538 Motuo suggest a weaker local biomass burning emissions. At urban Lhasa, four OA
539 factors were identified including an OOA with O/C ratio of 0.54 and three primary OA
540 components, i.e., BBOA (O/C of 0.13), cooking-related OA (COA, O/C of 0.12), and
541 HOA (O/C of 0.11). These components were markedly different from those at the above
542 remote sites with the three primary OA components accounting for more than 60% of
543 the total OA, suggesting the abundant primary aerosol sources from the residential
544 activities. In addition, the BBOA contribution increased significantly (up to 36%)
545 during a major local festival in Lhasa, suggesting the crucial aerosol source from
546 biomass burning during religious activities in the city (Zhao et al., 2022).
547 In summary, our study identified diverse OA components with varying O/C ratios at
548 different sites, indicating the heterogeneity of sources and oxidation states of OA across
549 the TP regions.

550 **4.5 Number concentrations of submicron aerosols and cloud condensation nuclei**
551 The measurement of particle number size distribution (PNSD) was useful for studying

552 the formation and growth mechanisms of aerosol particles in the atmosphere. Figure 7a
553 shows the high-resolution temporal variations of the PNSDs during four field
554 campaigns (QOMS, Motuo, LHG, and Lhasa), revealing significant variability in
555 number concentrations and size distribution patterns across the different sites. On
556 average, the total number concentration was 709.3 and 3994.4 cm^{-3} at QOMS and
557 Lhasa, respectively, while it was 1639.2 and 1462.0 cm^{-3} at Motuo and LHG. Notably,
558 the variations in particle number concentrations were not consistent with mass
559 concentrations measured from the HR-ToF-AMS at the four sites (Table 2). For instance,
560 although the PM_1 mass concentration at Lhasa was comparable to that at QOMS (4.7
561 versus 4.4 $\mu g\ m^{-3}$), the number concentration at Lhasa was more than five times higher
562 than that at QOMS. This inconsistency was mainly related to the difference on size
563 distribution at different sites. As mentioned above, submicron aerosols at QOMS were
564 predominantly secondary due to long-range transport from South Asia and
565 characterized by accumulation mode size. In contrast, Lhasa exhibited fresher aerosols,
566 emitted from local residential activities and characterized by Aitken mode size. The
567 variation in submicron aerosol sizes across the TP was further evidenced by the peak
568 diameters in the average mass and number size distributions (Figs. 4a and 7b). For
569 instance, the average OA mass size distribution peaked at 510.2 and 430.5 nm in D_{va}
570 for QOMS and Motuo, respectively. Meanwhile, the average number size distributions
571 at these two sites had peak at 109.4 and 131.0 nm in D_m. In contrast, Lhasa displayed
572 significantly smaller peak diameters of only 228.1 nm in D_{va} and 28.9 nm in D_m.

573 New particle formation (NPF) events were observed at several sites in our study.
574 Typically, an NPF event is characterized by a rapid burst in nucleation mode followed
575 by the subsequent growth into larger particles, as defined as banana-shaped temporal
576 developments in the PNSD (Dal Maso et al., 2005). Figure 7a displays the cases of
577 banana-shaped patterns in the PNSD, which were frequently observed at urban Lhasa.
578 Throughout the 27-day Lhasa campaign, a total of 10 NPF events were observed (Zhao
579 et al., 2022). In contrast, such banana-shaped pattern in the PNSD was relatively rare
580 at the other three remote sites (QOMS, Motuo, and LHG), which might be related to
581 their predominance of long-range transported aerosol with overall highly-aged states
582 and limited gaseous precursors.

583 Cloud condensation nuclei (CCN) is a distinct class of atmospheric aerosol particles
584 which could be activated as cloud droplets at a certain supersaturated water vapor

condition and played important roles in cloud formation, precipitation, climate change, and regional hydrological cycle (Andreae and Rosenfeld, 2008). Across the TP field campaigns, CCN measurements were conducted at three sites: Motuo, Waliguan, and LHG. The temporal variations of CCN number concentrations at each SS exhibited a similar trend with the total number concentration from the SMPS measurement and the PM_1 mass concentration from the HR-ToF-AMS measurement during each campaign. On average, the CCN number concentrations at Motuo were 974.0, 1142.6, 1240.1, 1296.5, and 1337.9 cm^{-3} at *SS* level of 0.2%, 0.4%, 0.6%, 0.8%, and 1.0%, respectively. At Waliguan, relatively comparable average values of 233.7, 857.8, 1138.7, 1313.1, and 1407.0 cm^{-3} were observed at corresponding SS levels. In contrast, LHG exhibited significantly lower average CCN concentration of 120.5, 340.1, 417.8, 468.0, and 504.5 cm^{-3} at the same *SS* levels, respectively (Table 2). The lower CCN number concentrations at LHG compared to Waliguan and Motuo were consistent with its lower PM_1 mass loading. Comparing with other regions, the CCN number concentrations at the three TP sites were almost an order of magnitude lower than those observed in polluted urban environments or from specific combustion emissions. For instance, CCN concentrations reached 12963 cm^{-3} (*SS* = 0.70%) in Wuqing, 9890 cm^{-3} (*SS* = 0.86%) in Beijing (Deng et al., 2011; Gunthe et al., 2011), 7913 cm^{-3} (*SS* = 0.70%) at Panyu in the Pearl River Delta, as well as 11565 cm^{-3} (*SS* = 0.87%) and 10000 cm^{-3} (*SS* = 0.80%) during unique biomass burning plumes (Rose et al., 2010; Zhang et al., 2020). However, the CCN values from our study were comparable to those measured at eight remote marine sites in the South China Sea (228−2150 cm^{-3} at *SS* = 0.87%) and the amazon rain forest (941 cm^{-3} at *SS* = 0.74%) (Pöhlker et al., 2016; Atwood et al., 2017). These comparisons again highlight the overall clean atmospheric condition in the TP.

4.6 Aerosol optical properties and light absorptions from BC and BrC

In this study, the parameters of B_{scat}, B_{abs}, and SSA of fine particles at 405 nm were observed at the field campaigns of QOMS, Motuo, Waliguan, Ngari, and Lhasa, to explore the variations in aerosol optical properties across the TP. On average, the B_{scat} and B_{abs} at 405 nm during the five campaigns were 121.9, 44.9, 36.3, 8.9, and 2.1 Mm^{-1} and 10.8, 7.0, 4.1, 3.6, and 1.9 Mm^{-1}, respectively. These values yielded average SSA values of 0.89, 0.83, 0.86, 0.67, and 0.52, correspondingly (Fig. 8a and Table 2). The B_{scat} and B_{abs} values at the TP sites were significantly lower than those reported in various urban areas in China, such as 459.5 and 47.2 Mm^{-1} at 630 nm in Beijing (Xie

et al., 2019), 272 and 31 Mm^{-1} at 532 nm in Xi'an (Zhu et al., 2015), and 418 and 91 Mm^{-1} at 540 nm in Guangzhou (Andreae et al., 2008), again suggesting the overall clean atmospheric condition in the TP. Although the PM_1 mass concentrations at QOMS was comparable to or even lower than those at the other four sites, QOMS exhibited the highest B_{scat}, B_{abs}, and SSA values. This discrepancy may be due to variations in aerosol chemical compositions and their mass scattering and absorbing efficiencies. In contrast, Lhasa exhibited a significantly lower SSA compared to the other four remote sites, suggesting a prevalence of fresh aerosols in the urban environment. On the other hand, aerosols at the four remote sites were highly aged, leading to significant photobleaching of BrC chromophores and an obvious decrease in their light absorptivity.

Real-time online measurements of particle B_{abs} at seven wavelengths ranging from 370 to 950 nm were also conducted using an aethalometer at QOMS, NamCo, and Waliguan, respectively, to explore regional variations in aerosol absorption properties across the TP. Overall, the muti-wavelength B_{abs} decreased significantly with the increasing wavelength during the three measurement campaigns, with fitted AAE values of 1.73, 1.28, and 1.12, respectively (Fig. 8b). The average B_{abs} at the shortest wavelength of 370 nm was 13.40, 3.25, and 2.66 Mm^{-1} at the three sites, respectively (Table 2). Despite a relatively low PM_1 mass concentrations at QOMS, the B_{abs} at 370 nm was five times higher than that at Waliguan, mainly due to a higher contribution of light-absorbing aerosol components in the southern TP. Specifically, OA and BC together accounted for nearly 80% of the total PM_1 at QOMS, whereas this contribution decreased to only 37.5% at Waliguan. The obviously higher AAE at QOMS also suggested a dominant light-absorbing contribution from BrC or the significant lensing effect of coated BC (Zhang et al., 2021). The inserted plots in Fig. 8b illustrate significant decreases in particle $B_{abs,BC}$ and $B_{abs,BrC}$ to total B_{abs} with increasing wavelength, yet their contributions to total B_{abs} ($fB_{abs,BC}$ and $fB_{abs,BrC}$) varied inversely. BC was the primary light-absorbing component across all the three sites, contributing 66.9%, 78.7%, and 77.6% to the total B_{abs} at 370 nm at QOMS, NamCo, and Waliguan sites, respectively; its contribution increased apparently with longer wavelengths (Table 2). Conversely, BrC showed more significant contributions to total B_{abs} at shorter wavelengths. For instance, the average $B_{abs,BrC}$ at 370 nm were 4.42, 0.69, and 0.60 Mm^{-1} at the three sites, respectively, ultimately contributing 33.1%, 21.3%, and 22.4% to the total B_{abs}. The significantly higher values of total B_{abs}, $B_{abs,BC}$, $B_{abs,BrC}$, and

651 $fB_{abs,BrC}$ in the southern TP region could be related to the important contributions of
652 light-absorbing CAs from transported biomass burning emissions (Xu et al., 2020,
653 2022).

654 **4.7 Estimation of aerosol radiative forcing in the different TP regions**

655 Atmospheric aerosols play a significant role in impacting Earth's climate systems
656 through affecting solar radiation and exerting a positive forcing on the energy budget
657 (Bond and Bergstrom, 2006). In this study, aerosol direct radiative forcings (DRF)
658 caused by BC, organic carbon (OC), and water-soluble ions (WSIs) are estimated,
659 respectively, using Santa Barbara DISORT (Discrete Ordinate Radiative Transfer)
660 Atmospheric Radiative Transfer (SBDART) model (Ricchiazzi et al., 1998). A detailed
661 introduction and operation of this model are described in Text S6 in the supplementary
662 material. Since the model's performance is evaluated and calibrated by comparing the
663 values with measurements from Aethalometer and PAX results, the aerosol DRF
664 estimations are limited to QOMS, NamCo, and Waliguan. Furthermore, these three sites
665 are located in the southern, central, and northern regions of the TP, respectively, which
666 allows for an exploration of regional variations in aerosol DRF across the TP.

667 Figure 9 presents the results of DRFs attributed to BC, OC, and WSIs across the three
668 campaigns. BC demonstrated a pronounced warming effect at the top of the atmosphere,
669 with average DRF values of +2.5 ± 0.5, +2.1 ± 0.1, and +1.9 ± 0.1 W m^{-2} during the
670 QOMS, Waliguan, and NamCo campaigns, respectively. In contrast, BC exhibited a
671 noticeable cooling effect at the earth's surface, with average DRF values of −4.7 ± 0.8,
672 −4.1 ± 0.2, and −3.7 ± 0.1 W m^{-2} across the three campaigns. The combination of these
673 two effects resulted in significantly high net atmospheric forcing by BC, amounting to
674 +7.3 ± 1.2, +6.2 ± 0.3, and +5.6 ± 0.2 W m^{-2} for the three campaigns. These results
675 suggest the important radiative effect of BC in the TP, especially in the southern region
676 influenced by long-range transported biomass burning emission from South Asia. In
677 contrast, OC and WSIs exhibited cooling effects at both the top of the atmosphere and
678 the Earth's surface, characterized by negative and relatively low average DRFs.
679 Consequently, the net atmospheric forcings for OC and WSIs were notably lower
680 compared to BC across the three campaigns, with values of +2.0 ± 1.2, +0.7 ± 0.2, and
681 +0.9 ± 0.7 W m^{-2} for OC, and +1.9 ± 0.8, +1.4 ± 0.6, and +1.2 ± 0.2 W m^{-2} for WSIs
682 at QOMS, Waliguan and NamCo, respectively. Interestingly, at QOMS, the average
683 atmospheric DRF of OC accounted for 27.3% of that of BC, whereas at Waliguan and

NamCo, the fractions were only 11.1% and 15.7%, respectively. The higher atmospheric DRF observed at QOMS suggests a dominant contribution from light-absorbing BC and BrC aerosols compared to Waliguan and NamCo.

It was worth noting that the simulations of DRF effects in this study were only conducted at three specific sites over limited periods. Future research should focus on long-term comprehensive measurements and DRF simulations across the entire TP to enhance our understanding of aerosol impacts on regional climate.

4.8 Long-range transport of aerosols from surrounding areas

To further understand the potential sources and specific transport pathways of aerosols at each site, particularly for those remote sites, three- or five-days air mass back trajectories were calculated during each measurement period at an ending height of 500 m above ground level every 6h using the Hybrid Single Particle Lagrangian Integrated Trajectory (HYSPLIT) model (Draxler and Rolph, 2003). The cluster analysis on the trajectories was based on the total spatial minimum variance method. Figure 10 displays the average backward trajectory clusters across all eight field campaigns.

In general, distinct air mass sources were identified across the TP. The five sites (QOMS, Motuo, Lhasa, NamCo, and Ngari) located in the southern or south-central part of the TP generally showed air masses from south or southwest with different transport distances and pathways during their measurement periods. For instance, during the QOMS campaign, 38% of the air masses originated from the west, covering a long distance, while another 40% originated from the southwest, covering a shorter distance. In the Motuo campaign, two major clusters both originated from the southwest with different distances (77% at shorter distance compared to only 13% at a longer distance). Similarly, during the NamCo campaign, two major clusters with comparable contributions (37% and 34%) and transport distances but different pathways were identified from the south. In the Ngari campaign, air masses showed similar transport distances, with 56% originating from southwest and 26% from the south. These air mass clusters originating from the south of the TP generally traverse polluted regions in South Asia such as the Indo-Gangetic Plain, Nepal, and Bangladesh, carrying significant amounts of pollutants, particularly biomass-burning emissions into the inland of the TP. In contrast, air masses at northern sites were primarily influenced by Westerlies and East Asian monsoon during summer season. In the campaigns of Bayanbulak, air

masses originated from the west with different distances, i.e., 69% in relatively shorter distance versus 18% in a longer distance. During the LHG campaign, the air masses originated from the northwest of the site with 63% in longer distance but 27% in shorter distance. For the Waliguan campaign, the air mass originated from two distinct directions. Most of air masses (57%) came from the northeast of the site with a shorter distance, while the remaining air masses originated from the west and northwest with longer distances.

In summary, significant variations in air mass sources and transport pathways were observed across the TP, particularly between southern and northern regions. These differences play a crucial role in shaping the different physiochemical and optical properties of aerosols across the TP regions.

5 Dataset limitations and applications

Our dataset was compiled from eight short-term intensive field observations across the TP utilizing a suite of high-resolution online instruments. However, it is important to note that our dataset does have certain limitations that proved to be quite challenging to address in these remote regions.

The primary limitation stems from the short and inconsistent measurement periods across different observational years and seasons at different sites, impeding robust comparisons of aerosol properties across the TP. This limitation also hampers the ability to ascertain long-term and seasonal characteristics. The harsh natural environments, challenging weather conditions, limited logistical support and instruments, and stringent instrumental requirements (such as the necessity for comprehensive field stations with stable power supply) presented significant challenges during our field observations in these remote TP regions. It is worth noting that online HR-ToF-AMS observations, such as the one we conducted, are predominantly short-term and intensive observations carried out worldwide due to the instability issues and its challenging maintenance required for long-term measurements. The short-term intensive measurement is enough to capture and characterize the dynamic evolution of aerosol properties at a high-time-resolution (Jimenez et al., 2009; Li et al., 2017). Long-term high-time-resolution observation utilizing HR-ToF-AMS have been rarely conducted thus far, even in urban environment with relatively favorable observational conditions and logistic support compared to our remote TP sites. Consequently, performing

continuous long-term observations or simultaneous comparison at multiple sites in these high-altitude remote TP regions, without stable power supply, is exceedingly challenging. Furthermore, assessing the representativeness of each observation for the spatial scale is particularly challenging due to the limited number of observatories across the TP. Actually, these observatories have been strategically established based on the representation of specific geographic and climatic features.

In addition to the limitations above, our team has made significant efforts to conduct this comprehensive observation project over the past decade, aiming to study the regional differences in aerosol sources and properties across the TP. The dataset generated from our project represents the first and exclusive high-time-resolution dataset focusing on atmospheric aerosol physicochemical and optical properties, covering most region of the TP. The applications of this dataset in atmospheric science are multifaceted. Firstly, the high-time-resolution observations offer crucial advantages in understanding the rapid evolution and diurnal variations of aerosol properties during a short period or special event. Furthermore, these observations are invaluable for model simulation and verification, providing a wealth of data points that can be utilized for assessing aerosol loading, chemical composition, size distribution, and other parameters essential for model accuracy and validation. Such advantages are not achievable with traditional off-line samplings, which typically exhibit low time resolutions ranging from days to weeks. Secondly, the eight sites encompassed in our project effectively represent a wide range of the TP. This is particularly noteworthy considering the limited availability of observatories on the TP. These sites facilitate comparisons of aerosol sources and properties among different regions. Thirdly, our observations encompass a wide range of aerosol physical, chemical, and optical parameters, including aerosol mass loadings, chemical compositions, size distribution, diurnal variations, number concentrations, light scattering and absorption coefficients, and so on. This comprehensive dataset plays a crucial role in fostering a profound understanding of aerosol properties in the TP.

Overall, it is noteworthy that our online observational aerosol datasets, focusing on multiple parameters with at least hourly-scale resolution at various sites across the TP, are the only ones reported to date.

6 Data availability

The high-resolution online measurement datasets, encompassing aerosol physical, chemical, and optical properties over the Tibetan Plateau and its surroundings in our observation project have been released and are now available for download from the National Cryosphere Desert Data Center (https://doi.org/10.12072/ncdc.NIEER.db2200.2022; Xu, 2022). These datasets are provided in an Excel file comprising eight worksheets. The first sheet of the Excel file contains a concise description of the dataset, including the dataset name, observation stations, sampling periods, online instruments used, and corresponding references. The remaining seven sheets present the high-resolution measurement data obtained from the online instruments employed during the eight campaigns. These instruments include HR-ToF-AMS, SMPS, PAX, aethalometer, and CCN-100.

7 Conclusions

This study presents a comprehensive dataset encompassing aerosol physicochemical and optical properties, with a particular focus on high-resolution size-resolved chemical characteristics and sources of submicron aerosols, conducted at eight different sites of the TP and its surroundings. The datasets collected offer insights into temporal and diurnal variations, size distribution of PM_1 chemical compositions, HRMS and chemical components of OA, particle light scattering and absorption coefficients, and CCN number concentrations at different supersaturations in different campaigns.

The datasets offer valuable insights into regional variations in aerosol properties and sources. In the southern TP region, atmospheric aerosols were primarily influenced by biomass burning emissions transported from South Asia, resulted in high mass contributions (>70%) of CAs and overall neutralized PM_1, as well as an enhanced light absorption capability of aerosols. In contrast, in the northern TP, secondary inorganic species, particularly sulfate, contributed significantly to total PM_1 due to the regional transport of anthropogenic aerosol and gaseous precursor emissions from urban areas in northwestern China. Furthermore, in contrast to the well-mixed, highly-aged, and regionally transported aerosols observed in the remote sites, atmospheric aerosols in the urban Lhasa were mainly originated from local primary sources such as cooking, traffic vehicle exhausts, and biofuel combustion during the residential activities. Consequently, these aerosol particles were relatively fresh, characterized by small size and low oxidation degree, but exhibited a high frequency of NPF origins.

Appendix A: Main Abbreviations

TP	Tibetan Plateau
HR-ToF-AMS	high-resolution time-of-flight aerosol mass spectrometer
SMPS	scanning mobility particle sizer
PAX	photo-acoustic extinctiometer
CCN	cloud condensation nuclei
SS	supersaturation
PM_1	submicron aerosol
BC	black carbon
BrC	brown carbon
OA	organic aerosol
SNA	sulfate, nitrate, and ammonium
D_m	mobility diameter
D_{va}	aerodynamic diameter
CE	collection efficiency
HRMS	high-resolution mass spectrum
PBL	planetary boundary layer
O/C	oxygen-to-carbon ratio
H/C	hydrogen-to-carbon ratio
N/C	nitrogen-to-carbon ratio
OM/OC	organic matter-to-organic carbon ratio
PMF	positive matrix factorization
OOA	oxygenated organic aerosol
LO-OOA	less oxidized oxygenated organic aerosol
MO-OOA	more oxidized oxygenated organic aerosol
BBOA	biomass-burning-related organic aerosol
agBBOA	aged biomass-burning-related organic aerosol
NOA	nitrogen-containing organic aerosol
HOA	traffic-related hydrocarbon-like organic aerosol
COA	cooking-related organic aerosol
PNSD	particle number size distribution
NPF	new particle formation
B_{scat}	light scattering coefficient
B_{abs}	light absorption coefficient
B_{ext}	light extinction coefficient
SSA	single scattering albedo
AAE	absorption Ångström exponents
$B_{abs,BC}$	light absorption coefficient from BC
$B_{abs,BrC}$	light absorption coefficient from BrC
OC	organic carbon
WSIs	water-soluble ions
DRF	direct radiative forcing

Author Contributions. JX designed the study, XZ, WZ, and JX wrote the manuscript. JX and SK organized and supervised the field measurement campaigns, JX, XZ, WZ, LZ, MZ, JS, JShi, YL, CX, YT, KL, XG, and QZ conducted the field measurements, JX, XZ, WZ, and YT analyzed the data. All authors reviewed and commented on the final form of the manuscript.

Competing interests. The authors declared that they have no competing interests.

Acknowledgements. We extend our thanks to all our colleagues and collaborators who participated the aerosol field measurements, maintained the instruments, analyzed the data, and commented on the manuscript. We also show great thanks to all the observation stations in this study for their logistical supports with the field campaigns.

Financial support. This work was supported by the National Natural Science Foundation of China (41977189, 41771079, 41805106), the Second Tibetan Plateau Scientific Expedition and Research program (STEP) (2019QZKK0605), the Strategic Priority Research Program of Chinese Academy of Sciences, Pan-Third Pole Environment Study for a Green Silk Road (Pan-TPE) (XDA20040501), the State Key Laboratory of Cryospheric Sciences Scientific Research Foundation (SKLCS-ZZ-2023), and the Chinese Academy of Sciences Hundred Talents Program.

References

Aiken, A. C., Salcedo, D., Cubison, M. J., Huffman, J. A., DeCarlo, P. F., Ulbrich, I. M., Docherty, K. S., Sueper, D., Kimmel, J. R., Worsnop, D. R., Trimborn, A., Northway, M., Stone, E. A., Schauer, J. J., Volkamer, R. M., Fortner, E., de Foy, B., Wang, J., Laskin, A., Shutthanandan, V., Zheng, J., Zhang, R., Gaffney, J., Marley, N. A., Paredes-Miranda, G., Arnott, W. P., Molina, L. T., Sosa, G., and Jimenez, J. L.: Mexico City aerosol analysis during MILAGRO using high resolution aerosol mass spectrometry at the urban supersite (T0) – Part 1: Fine particle composition and organic source apportionment, Atmos. Chem. Phys., 9, 6633-6653, https://doi.org/10.5194/acp-9-6633-2009, 2009.

Alfarra, M. R., Prevot, A. S. H., Szidat, S., Sandradewi, J., Weimer, S., Lanz, V. A., Schreiber, D., Mohr, M., and Baltensperger, U.: Identification of the mass spectral signature of organic aerosols from wood burning emissions, Environ. Sci. Technol., 41, 5770-5777, https://doi.org/10.1021/es062289b, 2007.

An, Y., Xu, J., Feng, L., Zhang, X., Liu, Y., Kang, S., Jiang, B., and Liao, Y.: Molecular characterization of organic aerosol in the Himalayas: insight from ultra-high-resolution mass spectrometry, Atmos. Chem. Phys., 19, 1115-1128, https://doi.org/10.5194/acp-19-1115-2019, 2019.

Andreae, M. O., and Rosenfeld, D.: Aerosol–cloud–precipitation interactions. Part 1. The nature and sources of cloud-active aerosols, Earth-Science Reviews, 89, 13-41, https://doi.org/10.1016/j.earscirev.2008.03.001, 2008.

Andreae, M. O., Schmid, O., Yang, H., Chand, D., Zhen Yu, J., Zeng, L.-M., and Zhang, Y.-H.: Optical properties and chemical composition of the atmospheric aerosol in urban Guangzhou, China, Atmos. Environ., 42, 6335-6350, https://doi.org/10.1016/j.atmosenv.2008.01.030, 2008.

Atwood, S. A., Reid, J. S., Kreidenweis, S. M., Blake, D. R., Jonsson, H. H., Lagrosas, N. D., Xian, P., Reid, E. A., Sessions, W. R., and Simpas, J. B.: Size-resolved aerosol and cloud condensation nuclei (CCN) properties in the remote marine South China Sea – Part 1: Observations and source classification, Atmos. Chem. Phys., 17, 1105-1123, https://doi.org/10.5194/acp-17-1105-2017, 2017.

Backman, J., Schmeisser, L., Virkkula, A., Ogren, J. A., Asmi, E., Starkweather, S., Sharma, S., Eleftheriadis, K., Uttal, T., Jefferson, A., Bergin, M., Makshtas, A., Tunved, P., and Fiebig, M.: On Aethalometer measurement uncertainties and an instrument correction factor for the Arctic, Atmos. Meas. Tech., 10, 5039–5062, https://doi.org/10.5194/amt-10-5039-2017, 2017.

Bonasoni, P., Laj, P., Marinoni, A., Sprenger, M., Angelini, F., Arduini, J., Bonafè, U., Calzolari, F., Colombo, T., Decesari, S., Di Biagio, C., di Sarra, A. G., Evangelisti, F., Duchi, R., Facchini, M. C., Fuzzi, S., Gobbi, G. P., Maione, M., Panday, A., Roccato, F., Sellegri, K., Venzac, H., Verza, G. P., Villani, P., Vuillermoz, E., and Cristofanelli, P.: Atmospheric Brown Clouds in the Himalayas: first two years of continuous observations at the Nepal Climate Observatory-Pyramid (5079 m), Atmos. Chem. Phys., 10, 7515-7531, https://doi.org/10.5194/acp-10-7515-2010, 2010.

Bond, T. C., and Bergstrom, R. W.: Light absorption by carbonaceous particles: An investigative review, Aerosol Sci. Technol., 40, 27-67, https://doi.org/10.1080/02786820500421521, 2006.
Canagaratna, M. R., Jimenez, J. L., Kroll, J. H., Chen, Q., Kessler, S. H., Massoli, P., Hildebrandt Ruiz, L., Fortner, E., Williams, L. R., Wilson, K. R., Surratt, J. D., Donahue, N. M., Jayne, J. T., and Worsnop, D. R.: Elemental ratio measurements of organic compounds using aerosol mass spectrometry: characterization, improved calibration, and implications, Atmos. Chem. Phys., 15, 253-272, https://doi.org/10.5194/acp-15-253-2015, 2015.
Cao, J., Xu, B., He, J., Liu, X., Han, Y., Wang, G., and Zhu, C.: Concentrations, seasonal variations, and transport of carbonaceous aerosols at a remote Mountainous region in western China, Atmos. Environ., 43, 4444-4452, https://doi.org/10.1016/j.atmosenv.2009.06.023, 2009.
Chen, F., Ding, L., Piao, S., Zhou, T., Xu, B., Yao, T., and Li, X.: The Tibetan Plateau as the engine for Asian environmental change: the Tibetan Plateau Earth system research into a new era, Science Bulletin, 66, 1263-1266, https://doi.org/10.1016/j.scib.2021.04.017, 2021.
Chen, P., Kang, S., Li, C., Zhang, Q., Guo, J., Tripathee, L., Zhang, Y., Li, G., Gul, C., Cong, Z., Wan, X., Niu, H., Panday, A. K., Rupakheti, M., and Ji, Z.: Carbonaceous aerosol characteristics on the Third Pole: A primary study based on the Atmospheric Pollution and Cryospheric Change (APCC) network, Environ. Pollut., 253, 49-60, https://doi.org/10.1016/j.envpol.2019.06.112, 2019.
Chen, Q., Heald, C. L., Jimenez, J. L., Canagaratna, M. R., Zhang, Q., He, L. Y., Huang, X. F., Campuzano-Jost, P., Palm, B. B., Poulain, L., Kuwata, M., Martin, S. T., Abbatt, J. P. D., Lee, A. K. Y., and Liggio, J.: Elemental composition of organic aerosol: The gap between ambient and laboratory measurements, Geophys. Res. Lett., 42, 4182-4189, https://doi.org/10.1002/2015gl063693, 2015.
Cong, Z., Kang, S., Kawamura, K., Liu, B., Wan, X., Wang, Z., Gao, S., and Fu, P.: Carbonaceous aerosols on the south edge of the Tibetan Plateau: concentrations, seasonality and sources, Atmos. Chem. Phys., 15, 1573-1584, https://doi.org/10.5194/acp-15-1573-2015, 2015.
Cui, Y. Y., Liu, S., Bai, Z., Bian, J., Li, D., Fan, K., McKeen, S. A., Watts, L. A., Ciciora, S. J., and Gao, R.-S.: Religious burning as a potential major source of atmospheric fine aerosols in summertime Lhasa on the Tibetan Plateau, Atmos. Environ., 181, 186-191, https://doi.org/10.1016/j.atmosenv.2018.03.025, 2018.
Dal Maso, M., Kulmala, M., Riipinen, I., Wagner, R., Hussein, T., Aalto, P. P., and Lehtinen, K. E. J.: Formation and growth of fresh atmospheric aerosols: eight years of aerosol size distribution data from SMEAR II, Hyytiala, Finland, Boreal Environ. Res., 10, 323-336, 2005.
Deng, Z. Z., Zhao, C. S., Ma, N., Liu, P. F., Ran, L., Xu, W. Y., Chen, J., Liang, Z., Liang, S., Huang, M. Y., Ma, X. C., Zhang, Q., Quan, J. N., Yan, P., Henning, S., Mildenberger, K., Sommerhage, E., Schäfer, M., Stratmann, F., and Wiedensohler, A.: Size-resolved and bulk activation properties of aerosols in the North China Plain, Atmos. Chem. Phys., 11, 3835-3846, https://doi.org/10.5194/acp-11-3835-2011, 2011.
Draxler, R. R., and Rolph, G. D.: HYSPLIT (HYbrid Single-Particle Lagrangian Integrated Trajectory) model access via NOAA ARL READY website (http://www.arl.noaa.gov/ready/hysplit4.html). in, NOAA Air Resources Laboratory, Silver Spring, MD, USA, 2003.
Du, W., Sun, Y. L., Xu, Y. S., Jiang, Q., Wang, Q. Q., Yang, W., Wang, F., Bai, Z. P., Zhao, X. D., and Yang, Y. C.: Chemical characterization of submicron aerosol and particle growth events at a national background site (3295 m a.s.l.) on the Tibetan Plateau, Atmos. Chem. Phys., 15, 10811-10824, https://doi.org/10.5194/acp-15-10811-2015, 2015.
Duan, A. M., and Wu, G. X.: Role of the Tibetan Plateau thermal forcing in the summer climate patterns over subtropical Asia, Clim. Dyn., 24, 793-807, https://doi.org/10.1007/s00382-004-0488-8, 2005.
Freney, E. J., Sellegri, K., Canonaco, F., Boulon, J., Hervo, M., Weigel, R., Pichon, J. M., Colomb, A., Prévôt, A. S. H., and Laj, P.: Seasonal variations in aerosol particle composition at the puy-de-Dôme research station in France, Atmos. Chem. Phys., 11, 13047-13059, https://doi.org/10.5194/acp-11-13047-2011, 2011.
Fröhlich, R., Cubison, M. J., Slowik, J. G., Bukowiecki, N., Canonaco, F., Croteau, P. L., Gysel, M., Henne, S., Herrmann, E., Jayne, J. T., Steinbacher, M., Worsnop, D. R., Baltensperger, U., and Prévôt, A. S. H.: Fourteen months of on-line measurements of the non-refractory submicron aerosol at the Jungfraujoch (3580 m a.s.l.) – chemical composition, origins and organic aerosol sources, Atmos. Chem. Phys., 15, 11373-11398, https://doi.org/10.5194/acp-15-11373-2015, 2015.
Gunthe, S. S., Rose, D., Su, H., Garland, R. M., Achtert, P., Nowak, A., Wiedensohler, A., Kuwata, M., Takegawa, N., Kondo, Y., Hu, M., Shao, M., Zhu, T., Andreae, M. O., and Pöschl, U.: Cloud condensation nuclei (CCN) from fresh and aged air pollution in the megacity region of Beijing, Atmos. Chem. Phys., 11, 11023-11039, https://doi.org/10.5194/acp-11-11023-2011, 2011.
He, L. Y., Lin, Y., Huang, X. F., Guo, S., Xue, L., Su, Q., Hu, M., Luan, S. J., and Zhang, Y. H.: Characterization of high-resolution aerosol mass spectra of primary organic aerosol emissions from

Chinese cooking and biomass burning, Atmos. Chem. Phys., 10, 11535-11543, https://doi.org/10.5194/acp-10-11535-2010, 2010.
Jimenez, J. L., Canagaratna, M. R., Donahue, N. M., Prevot, A. S., Zhang, Q., Kroll, J. H., DeCarlo, P. F., Allan, J. D., Coe, H., Ng, N. L., Aiken, A. C., Docherty, K. S., Ulbrich, I. M., Grieshop, A. P., Robinson, A. L., Duplissy, J., Smith, J. D., Wilson, K. R., Lanz, V. A., Hueglin, C., Sun, Y. L., Tian, J., Laaksonen, A., Raatikainen, T., Rautiainen, J., Vaattovaara, P., Ehn, M., Kulmala, M., Tomlinson, J. M., Collins, D. R., Cubison, M. J., Dunlea, E. J., Huffman, J. A., Onasch, T. B., Alfarra, M. R., Williams, P. I., Bower, K., Kondo, Y., Schneider, J., Drewnick, F., Borrmann, S., Weimer, S., Demerjian, K., Salcedo, D., Cottrell, L., Griffin, R., Takami, A., Miyoshi, T., Hatakeyama, S., Shimono, A., Sun, J. Y., Zhang, Y. M., Dzepina, K., Kimmel, J. R., Sueper, D., Jayne, J. T., Herndon, S. C., Trimborn, A. M., Williams, L. R., Wood, E. C., Middlebrook, A. M., Kolb, C. E., Baltensperger, U., and Worsnop, D. R.: Evolution of organic aerosols in the atmosphere, Science, 326, 1525-1529, https://doi.org/10.1126/science.1180353, 2009.
Jimenez, J. L., Canagaratna, M. R., Drewnick, F., Allan, J. D., Alfarra, M. R., Middlebrook, A. M., Slowik, J. G., Zhang, Q., Coe, H., Jayne, J. T., and Worsnop, D. R.: Comment on "The Effects of Molecular Weight and Thermal Decomposition on the Sensitivity of a Thermal Desorption Aerosol Mass Spectrometer". Aerosol Sci. Technol., 50(9), i–xv, http://doi:10.1080/02786826.2016.1205728, 2016.
Kang, S., Xu, Y., You, Q., Flügel, W.-A., Pepin, N., and Yao, T.: Review of climate and cryospheric change in the Tibetan Plateau, Environ. Res. Lett., 5, 015101, https://doi.org/10.1088/1748-9326/5/1/015101, 2010.
Kang, S., Chen, P., Li, C., Liu, B., and Cong, Z.: Atmospheric Aerosol Elements over the Inland Tibetan Plateau: Concentration, Seasonality, and Transport, Aerosol Air Qual. Res., 16, 789-800, https://doi.org/10.4209/aaqr.2015.05.0307, 2016.
Kang, S., Cong, Z., Wang, X., Zhang, Q., Ji, Z., Zhang, Y., and Xu, B.: The transboundary transport of air pollutants and their environmental impacts on Tibetan Plateau, Chin. Sci. Bull., 64, 2876-2884, https://doi.org/10.1360/tb-2019-0135, 2019a.
Kang, S., Zhang, Q., Qian, Y., Ji, Z., Li, C., Cong, Z., Zhang, Y., Guo, J., Du, W., Huang, J., You, Q., Panday, A. K., Rupakheti, M., Chen, D., Gustafsson, Ö., Thiemens, M. H., and Qin, D.: Linking atmospheric pollution to cryospheric change in the Third Pole region: current progress and future prospects, Natl. Sci. Rev., 6, 796-809, https://doi.org/10.1093/nsr/nwz031, 2019b.
Kang, S., Zhang, Y., Chen, P., Guo, J., Zhang, Q., Cong, Z., Kaspari, S., Tripathee, L., Gao, T., Niu, H., Zhong, X., Chen, X., Hu, Z., Li, X., Li, Y., Neupane, B., Yan, F., Rupakheti, D., Gul, C., Zhang, W., Wu, G., Yang, L., Wang, Z., and Li, C.: Black carbon and organic carbon dataset over the Third Pole, Earth System Science Data, 14, 683-707, https://doi.org/10.5194/essd-14-683-2022, 2022.
Kopacz, M., Mauzerall, D. L., Wang, J., Leibensperger, E. M., Henze, D. K., and Singh, K.: Origin and radiative forcing of black carbon transported to the Himalayas and Tibetan Plateau, Atmos. Chem. Phys., 11, 2837-2852, https://doi.org/10.5194/acp-11-2837-2011, 2011.
Lau, K. M., Kim, M. K., and Kim, K. M.: Asian summer monsoon anomalies induced by aerosol direct forcing: the role of the Tibetan Plateau, Clim. Dyn., 26, 855-864, https://doi.org/10.1007/s00382-006-0114-z, 2006.
Li, C., Bosch, C., Kang, S., Andersson, A., Chen, P., Zhang, Q., Cong, Z., Chen, B., Qin, D., and Gustafsson, O.: Sources of black carbon to the Himalayan-Tibetan Plateau glaciers, Nat. Commun., 7, 12574, https://doi.org/10.1038/ncomms12574, 2016a.
Li, C., Yan, F., Kang, S., Chen, P., Hu, Z., Gao, S., Qu, B., and Sillanpää, M.: Light absorption characteristics of carbonaceous aerosols in two remote stations of the southern fringe of the Tibetan Plateau, China, Atmos. Environ., 143, 79-85, https://doi.org/10.1016/j.atmosenv.2016.08.042, 2016b.
Li, X., Kang, S., Zhang, G., Qu, B., Tripathee, L., Paudyal, R., Jing, Z., Zhang, Y., Yan, F., Li, G., Cui, X., Xu, R., Hu, Z., and Li, C.: Light-absorbing impurities in a southern Tibetan Plateau glacier: Variations and potential impact on snow albedo and radiative forcing, Atmos. Res., 200, 77-87, https://doi.org/10.1016/j.atmosres.2017.10.002, 2018.
Li, Y. J., Sun, Y., Zhang, Q., Li, X., Li, M., Zhou, Z., and Chan, C. K.: Real-time chemical characterization of atmospheric particulate matter in China: A review, Atmos. Environ., 158, 270-304, https://doi.org/10.1016/j.atmosenv.2017.02.027, 2017.
Liu, Y., Sato, Y., Jia, R., Xie, Y., Huang, J., and Nakajima, T.: Modeling study on the transport of summer dust and anthropogenic aerosols over the Tibetan Plateau, Atmos. Chem. Phys., 15, 12581-12594, https://doi.org/10.5194/acp-15-12581-2015, 2015.
Liu, Y., Hua, S., Jia, R., and Huang, J.: Effect of Aerosols on the Ice Cloud Properties Over the Tibetan Plateau, J. Geophys. Res. Atmos., 124, 9594-9608, https://doi.org/10.1029/2019jd030463, 2019.
Middlebrook, A. M., Bahreini, R., Jimenez, J. L., and Canagaratna, M. R.: Evaluation of Composition-Dependent Collection Efficiencies for the Aerodyne Aerosol Mass Spectrometer using Field Data,

Aerosol Sci. Technol., 46, 258-271, https://doi.org/10.1080/02786826.2011.620041, 2012.
Pöhlker, M. L., Pöhlker, C., Ditas, F., Klimach, T., Hrabe de Angelis, I., Araújo, A., Brito, J., Carbone, S., Cheng, Y., Chi, X., Ditz, R., Gunthe, S. S., Kesselmeier, J., Könemann, T., Lavrič, J. V., Martin, S. T., Mikhailov, E., Moran-Zuloaga, D., Rose, D., Saturno, J., Su, H., Thalman, R., Walter, D., Wang, J., Wolff, S., Barbosa, H. M. J., Artaxo, P., Andreae, M. O., and Pöschl, U.: Long-term observations of cloud condensation nuclei in the Amazon rain forest – Part 1: Aerosol size distribution, hygroscopicity, and new model parametrizations for CCN prediction, Atmos. Chem. Phys., 16, 15709-15740, https://doi.org/10.5194/acp-16-15709-2016, 2016.
Qiu, J.: The third pole, Nature, 454, 393-396, https://doi.org/10.1038/454393a, 2008.
Ramanathan, V., Ramana, M. V., Roberts, G., Kim, D., Corrigan, C., Chung, C., and Winker, D.: Warming trends in Asia amplified by brown cloud solar absorption, Nature, 448, 575-578, https://doi.org/10.1038/nature06019, 2007.
Ricchiazzi, P., Yang, S., Gautier, C., and Sowle, D.: SBDART: A Research and Teaching Software Tool for Plane-Parallel Radiative Transfer in the Earth's Atmosphere, Bull. Am. Meteorol. Soc., 79, 2101-2114, https://doi.org/10.1175/1520-0477(1998)079<2101:Sarats>2.0.Co;2, 1998.
Rinaldi, M., Gilardoni, S., Paglione, M., Sandrini, S., Fuzzi, S., Massoli, P., Bonasoni, P., Cristofanelli, P., Marinoni, A., Poluzzi, V., and Decesari, S.: Organic aerosol evolution and transport observed at Mt. Cimone (2165 m a.s.l.), Italy, during the PEGASOS campaign, Atmos. Chem. Phys., 15, 11327-11340, https://doi.org/10.5194/acp-15-11327-2015, 2015.
Rose, D., Gunthe, S. S., Mikhailov, E., Frank, G. P., Dusek, U., Andreae, M. O., and Pöschl, U.: Calibration and measurement uncertainties of a continuous-flow cloud condensation nuclei counter (DMT-CCNC): CCN activation of ammonium sulfate and sodium chloride aerosol particles in theory and experiment, Atmos. Chem. Phys., 8, 1153–1179, https://doi.org/10.5194/acp-8-1153-2008, 2008.
Rose, D., Nowak, A., Achtert, P., Wiedensohler, A., Hu, M., Shao, M., Zhang, Y., Andreae, M. O., and Poschl, U.: Cloud condensation nuclei in polluted air and biomass burning smoke near the mega-city Guangzhou, China - Part 1: Size-resolved measurements and implications for the modeling of aerosol particle hygroscopicity and CCN activity, Atmos. Chem. Phys., 10, 3365-3383, https://doi.org/10.5194/acp-10-3365-2010, 2010.
Schmale, J., Schneider, J., Nemitz, E., Tang, Y. S., Dragosits, U., Blackall, T. D., Trathan, P. N., Phillips, G. J., Sutton, M., and Braban, C. F.: Sub-Antarctic marine aerosol: dominant contributions from biogenic sources, Atmos. Chem. Phys., 13, 8669-8694, https://doi.org/10.5194/acp-13-8669-2013, 2013.
Schueneman, M. K., Nault, B. A., Campuzano-Jost, P., Jo, D. S., Day, D. A., Schroder, J. C., Palm, B. B., Hodzic, A., Dibb, J. E., and Jimenez, J. L.: Aerosol pH indicator and organosulfate detectability from aerosol mass spectrometry measurements, Atmos. Meas. Tech., 14, 2237-2260, https://doi.org/10.5194/amt-14-2237-2021, 2021.
Selimovic, V., Yokelson, R. J., Warneke, C., Roberts, J. M., de Gouw, J., Reardon, J., and Griffith, D. W. T.: Aerosol optical properties and trace gas emissions by PAX and OP-FTIR for laboratory-simulated western US wildfires during FIREX, Atmos. Chem. Phys., 18, 2929–2948, https://doi.org/10.5194/acp-18-2929-2018, 2018.
Sun, Y. L., Zhang, Q., Macdonald, A. M., Hayden, K., Li, S. M., Liggio, J., Liu, P. S. K., Anlauf, K. G., Leaitch, W. R., Steffen, A., Cubison, M., Worsnop, D. R., van Donkelaar, A., and Martin, R. V.: Size-resolved aerosol chemistry on Whistler Mountain, Canada with a high-resolution aerosol mass spectrometer during INTEX-B, Atmos. Chem. Phys., 9, 3095-3111, https://doi.org/10.5194/acp-9-3095-2009, 2009.
Sun, Y. L., Zhang, Q., Schwab, J. J., Demerjian, K. L., Chen, W. N., Bae, M. S., Hung, H. M., Hogrefe, O., Frank, B., Rattigan, O. V., and Lin, Y. C.: Characterization of the sources and processes of organic and inorganic aerosols in New York city with a high-resolution time-of-flight aerosol mass apectrometer, Atmos. Chem. Phys., 11, 1581-1602, https://doi.org/10.5194/acp-11-1581-2011, 2011.
Takami, A., Miyoshi, T., Shimono, A., and Hatakeyama, S.: Chemical composition of fine aerosol measured by AMS at Fukue Island, Japan during APEX period, Atmos. Environ., 39, 4913-4924, https://doi.org/10.1016/j.atmosenv.2005.04.038, 2005.
Van Damme, M., Erisman, J. W., Clarisse, L., Dammers, E., Whitburn, S., Clerbaux, C., Dolman, A. J., and Coheur, P.-F.: Worldwide spatiotemporal atmospheric ammonia (NH_3) columns variability revealed by satellite, Geophys. Res. Lett., 42, 8660-8668, https://doi.org/10.1002/2015gl065496, 2015.
Wan, X., Kang, S., Wang, Y., Xin, J., Liu, B., Guo, Y., Wen, T., Zhang, G., and Cong, Z.: Size distribution of carbonaceous aerosols at a high-altitude site on the central Tibetan Plateau (Nam Co Station, 4730ma.s.l.), Atmos. Res., 153, 155-164, https://doi.org/10.1016/j.atmosres.2014.08.008, 2015.
Wang, J., Ge, X., Chen, Y., Shen, Y., Zhang, Q., Sun, Y., Xu, J., Ge, S., Yu, H., and Chen, M.: Highly time-resolved urban aerosol characteristics during springtime in Yangtze River Delta, China: insights

from soot particle aerosol mass spectrometry, Atmos. Chem. Phys., 16, 9109-9127, https://doi.org/10.5194/acp-16-9109-2016, 2016.
Wang, J., Zhang, Q., Chen, M., Collier, S., Zhou, S., Ge, X., Xu, J., Shi, J., Xie, C., Hu, J., Ge, S., Sun, Y., and Coe, H.: First Chemical Characterization of Refractory Black Carbon Aerosols and Associated Coatings over the Tibetan Plateau (4730 m a.s.l), Environ. Sci. Technol., 51, 14072-14082, https://doi.org/10.1021/acs.est.7b03973, 2017.
Xie, C., Xu, W., Wang, J., Wang, Q., Liu, D., Tang, G., Chen, P., Du, W., Zhao, J., Zhang, Y., Zhou, W., Han, T., Bian, Q., Li, J., Fu, P., Wang, Z., Ge, X., Allan, J., Coe, H., and Sun, Y.: Vertical characterization of aerosol optical properties and brown carbon in winter in urban Beijing, China, Atmos. Chem. Phys., 19, 165-179, https://doi.org/10.5194/acp-19-165-2019, 2019.
Xu, B., Cao, J., Hansen, J., Yao, T., Joswia, D. R., Wang, N., Wu, G., Wang, M., Zhao, H., Yang, W., Liu, X., and He, J.: Black soot and the survival of Tibetan glaciers, Proc. Natl. Acad. Sci. USA, 106, 22114-22118, https://doi.org/10.1073/pnas.0910444106, 2009.
Xu, J., Wang, Z., Yu, G., Qin, X., Ren, J., and Qin, D.: Characteristics of water soluble ionic species in fine particles from a high altitude site on the northern boundary of Tibetan Plateau: Mixture of mineral dust and anthropogenic aerosol, Atmos. Res., 143, 43-56, https://doi.org/10.1016/j.atmosres.2014.01.018, 2014a.
Xu, J., Zhang, Q., Chen, M., Ge, X., Ren, J., and Qin, D.: Chemical composition, sources, and processes of urban aerosols during summertime in northwest China: insights from high-resolution aerosol mass spectrometry, Atmos. Chem. Phys., 14, 12593-12611, https://doi.org/10.5194/acp-14-12593-2014, 2014b.
Xu, J., Zhang, Q., Wang, Z. B., Yu, G. M., Ge, X. L., and Qin, X.: Chemical composition and size distribution of summertime $PM_{2.5}$ at a high altitude remote location in the northeast of the Qinghai-Xizang (Tibet) Plateau: insights into aerosol sources and processing in free troposphere, Atmos. Chem. Phys., 15, 5069-5081, https://doi.org/10.5194/acp-15-5069-2015, 2015.
Xu, J., Shi, J., Zhang, Q., Ge, X., Canonaco, F., Prévôt, A. S. H., Vonwiller, M., Szidat, S., Ge, J., Ma, J., An, Y., Kang, S., and Qin, D.: Wintertime organic and inorganic aerosols in Lanzhou, China: sources, processes, and comparison with the results during summer, Atmos. Chem. Phys., 16, 14937-14957, https://doi.org/10.5194/acp-16-14937-2016, 2016.
Xu, J., Zhang, Q., Shi, J., Ge, X., Xie, C., Wang, J., Kang, S., Zhang, R., and Wang, Y.: Chemical characteristics of submicron particles at the central Tibetan Plateau: insights from aerosol mass spectrometry, Atmos. Chem. Phys., 18, 427-443, https://doi.org/10.5194/acp-18-427-2018, 2018.
Xu, J., Hettiyadura, A. P. S., Liu, Y., Zhang, X., Kang, S., and Laskin, A.: Regional Differences of Chemical Composition and Optical Properties of Aerosols in the Tibetan Plateau, J. Geophys. Res. Atmos., 125, https://doi.org/10.1029/2019jd031226, 2020.
Xu, J.: High-time-resolution dataset of atmospheric aerosols over the Tibetan Plateau and its surroundings (2015-2021), National Cryosphere Desert Data Center [Data set], https://doi.org/10.12072/ncdc.NIEER.db2200.2022, 2022.
Xu, J., Hettiyadura, A. P. S., Liu, Y., Zhang, X., Kang, S., and Laskin, A.: Atmospheric Brown Carbon on the Tibetan Plateau: Regional Differences in Chemical Composition and Light Absorption Properties, Environmental Science & Technology Letters, 9, 219-225, https://doi.org/10.1021/acs.estlett.2c00016, 2022.
Yao, T., Thompson, L., Mosbrugger, V., Zhang, F., Ma, Y., Luo, T., Xu, B., Yang, X., Joswiak, D. R., Wang, W., Joswiak, M. E., Devkota, L. P., Tayal, S., Jilani, R., and Fayziev, R.: Third Pole Environment (TPE), Environ. Dev., 3, 52-64, https://doi.org/10.1016/j.envdev.2012.04.002, 2012.
Yao, T., Xue, Y., Chen, D., Chen, F., Thompson, L., Cui, P., Koike, T., Lau, W. K. M., Lettenmaier, D., Mosbrugger, V., Zhang, R., Xu, B., Dozier, J., Gillespie, T., Gu, Y., Kang, S., Piao, S., Sugimoto, S., Ueno, K., Wang, L., Wang, W., Zhang, F., Sheng, Y., Guo, W., Ailikun, Yang, X., Ma, Y., Shen, S. S. P., Su, Z., Chen, F., Liang, S., Liu, Y., Singh, V. P., Yang, K., Yang, D., Zhao, X., Qian, Y., Zhang, Y., and Li, Q.: Recent Third Pole's Rapid Warming Accompanies Cryospheric Melt and Water Cycle Intensification and Interactions between Monsoon and Environment: Multidisciplinary Approach with Observations, Modeling, and Analysis, Bull. Am. Meteorol. Soc., 100, 423-444, https://doi.org/10.1175/bams-d-17-0057.1, 2019.
You, Q., Cai, Z., Pepin, N., Chen, D., Ahrens, B., Jiang, Z., Wu, F., Kang, S., Zhang, R., Wu, T., Wang, P., Li, M., Zuo, Z., Gao, Y., Zhai, P., and Zhang, Y.: Warming amplification over the Arctic Pole and Third Pole: Trends, mechanisms and consequences, Earth-Science Reviews, 217, 103625, https://doi.org/10.1016/j.earscirev.2021.103625, 2021.
Zhang, N., Cao, J., Liu, S., Zhao, Z., Xu, H., and Xiao, S.: Chemical composition and sources of $PM_{2.5}$ and TSP collected at Qinghai Lake during summertime, Atmos. Res., 138, 213-222, https://doi.org/10.1016/j.atmosres.2013.11.016, 2014.

Zhang, Q., Alfarra, M. R., Worsnop, D. R., Allan, J. D., Coe, H., Canagaratna, M. R., and Jimenez, J. L.: Deconvolution and quantification of hydrocarbon-like and oxygenated organic aerosols based on aerosol mass spectrometry, Environ. Sci. Technol., 39, 4938-4952, https://doi.org/10.1021/es048568l, 2005a.
Zhang, Q., Canagaratna, M. R., Jayne, J. T., Worsnop, D. R., and Jimenez, J. L.: Time- and size-resolved chemical composition of submicron particles in Pittsburgh: Implications for aerosol sources and processes, J. Geophys. Res. Atmos., 110, D07S09, https://doi.org/10.1029/2004jd004649, 2005b.
Zhang, Q., Jimenez, J. L., Canagaratna, M. R., Allan, J. D., Coe, H., Ulbrich, I., Alfarra, M. R., Takami, A., Middlebrook, A. M., Sun, Y. L., Dzepina, K., Dunlea, E., Docherty, K., DeCarlo, P. F., Salcedo, D., Onasch, T., Jayne, J. T., Miyoshi, T., Shimono, A., Hatakeyama, S., Takegawa, N., Kondo, Y., Schneider, J., Drewnick, F., Borrmann, S., Weimer, S., Demerjian, K., Williams, P., Bower, K., Bahreini, R., Cottrell, L., Griffin, R. J., Rautiainen, J., Sun, J. Y., Zhang, Y. M., and Worsnop, D. R.: Ubiquity and dominance of oxygenated species in organic aerosols in anthropogenically-influenced Northern Hemisphere midlatitudes, Geophys. Res. Lett., 34, L13801, https://doi.org/10.1029/2007gl029979, 2007a.
Zhang, Q., Jimenez, J. L., Worsnop, D., and Canagaratna, M.: A case study of urban particle acidity and its influence on secondary organic aerosol, Environ. Sci. Technol., 41, 3213-3219, https://doi.org/10.1021/es061812j, 2007b.
Zhang, X., Xu, J., Kang, S., Liu, Y., and Zhang, Q.: Chemical characterization of long-range transport biomass burning emissions to the Himalayas: insights from high-resolution aerosol mass spectrometry, Atmos. Chem. Phys., 18, 4617–4638, https://doi.org/10.5194/acp-18-4617-2018, 2018.
Zhang, X., Xu, J., Kang, S., Zhang, Q., and Sun, J.: Chemical characterization and sources of submicron aerosols in the northeastern Qinghai–Tibet Plateau: insights from high-resolution mass spectrometry, Atmos. Chem. Phys., 19, 7897-7911, https://doi.org/10.5194/acp-19-7897-2019, 2019.
Zhang, X., Xu, J., and Kang, S.: Chemical characterization of submicron particulate matter (PM_1) emitted by burning highland barley in the northeastern part of the Qinghai–Tibet Plateau, Atmos. Environ., 224, 117351, https://doi.org/10.1016/j.atmosenv.2020.117351, 2020.
Zhang, X., Xu, J., Kang, S., Sun, J., Shi, J., Gong, C., Sun, X., Du, H., Ge, X., and Zhang, Q.: Regional Differences in the Light Absorption Properties of Fine Particulate Matter Over the Tibetan Plateau: Insights From HR-ToF-AMS and Aethalometer Measurements, J. Geophys. Res. Atmos., 126, https://doi.org/10.1029/2021jd035562, 2021.
Zhao, W., Zhang, X., Zhai, L., Shen, X., and Xu, J.: Chemical characterization and sources of submicron aerosols in Lhasa on the Qinghai–Tibet Plateau: Insights from high-resolution mass spectrometry, Sci. Total Environ., 815, https://doi.org/10.1016/j.scitotenv.2021.152866, 2022.
Zhao, Z., Cao, J., Shen, Z., Xu, B., Zhu, C., Chen, L.-W. A., Su, X., Liu, S., Han, Y., Wang, G., and Ho, K.: Aerosol particles at a high-altitude site on the Southeast Tibetan Plateau, China: Implications for pollution transport from South Asia, J. Geophys. Res. Atmos., 118, 11360-11375, https://doi.org/10.1002/jgrd.50599, 2013.
Zheng, J., Hu, M., Du, Z., Shang, D., Gong, Z., Qin, Y., Fang, J., Gu, F., Li, M., Peng, J., Li, J., Zhang, Y., Huang, X., He, L., Wu, Y., and Guo, S.: Influence of biomass burning from South Asia at a high-altitude mountain receptor site in China, Atmos. Chem. Phys., 17, 6853-6864, https://doi.org/10.5194/acp-17-6853-2017, 2017.
Zhou, S., Collier, S., Jaffe, D. A., Briggs, N. L., Hee, J., Sedlacek Iii, A. J., Kleinman, L., Onasch, T. B., and Zhang, Q.: Regional influence of wildfires on aerosol chemistry in the western US and insights into atmospheric aging of biomass burning organic aerosol, Atmos. Chem. Phys., 17, 2477-2493, https://doi.org/10.5194/acp-17-2477-2017, 2017.
Zhou, T., and Zhang, W.: Anthropogenic warming of Tibetan Plateau and constrained future projection, Environ. Res. Lett., 16, 044039, https://doi.org/10.1088/1748-9326/abede8, 2021.
Zhou, W., Xu, W., Kim, H., Zhang, Q., Fu, P., Worsnop, D. R., and Sun, Y.: A review of aerosol chemistry in Asia: insights from aerosol mass spectrometer measurements, Environ. Sci.: Proc. Imp., https://doi.org/10.1039/D0EM00212G, 2020.
Zhu, C.-S., Cao, J.-J., Ho, K.-F., Antony Chen, L. W., Huang, R.-J., Wang, Y.-C., Li, H., Shen, Z.-X., Chow, J. C., Watson, J. G., Su, X.-l., Wang, Q.-y., and Xiao, S.: The optical properties of urban aerosol in northern China: A case study at Xi'an, Atmos. Res., 160, 59-67, https://doi.org/10.1016/j.atmosres.2015.03.008, 2015.
Zhu, Q., He, L. Y., Huang, X. F., Cao, L. M., Gong, Z. H., Wang, C., Zhuang, X., and Hu, M.: Atmospheric aerosol compositions and sources at two national background sites in northern and southern China, Atmos. Chem. Phys., 16, 10283-10297, https://doi.org/10.5194/acp-16-10283-2016, 2016.

Figures

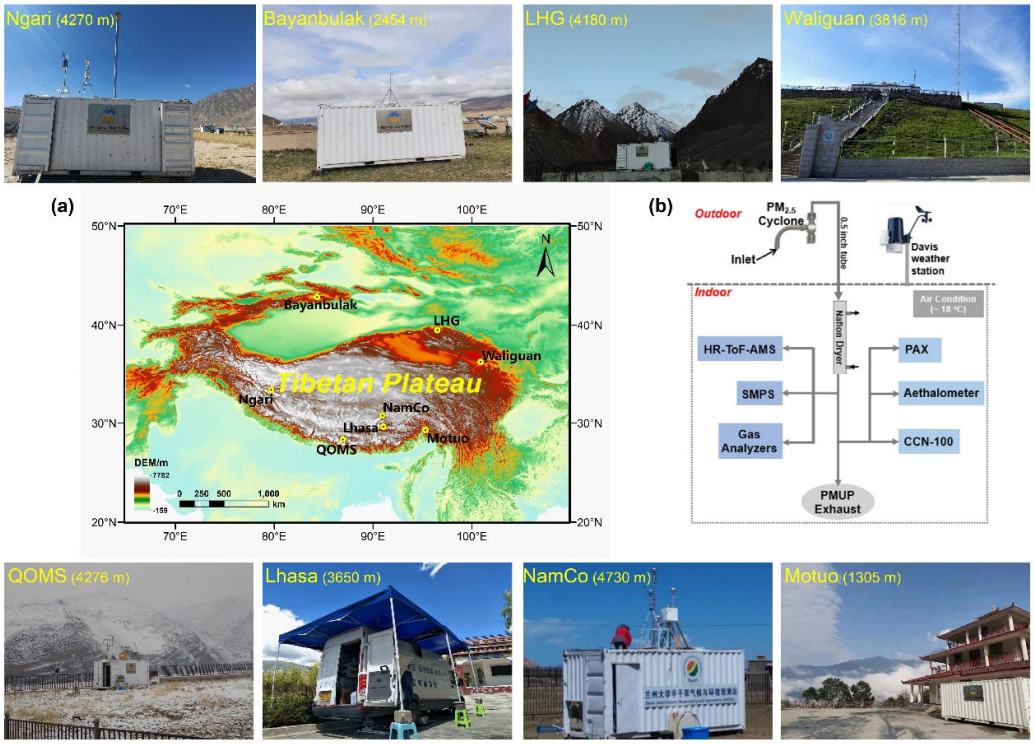

Figure 1. (a) Geographical locations of the observation sites (see Table 1 for full name and characteristics of each site) in the Tibetan Plateau and its surroundings in this study (The geographical base map is created with ArcGIS). Fieldwork photographs illustrate the real observation conditions and surroundings at each site. **(b)** The normal sampling setups of instruments during the online aerosol observations.

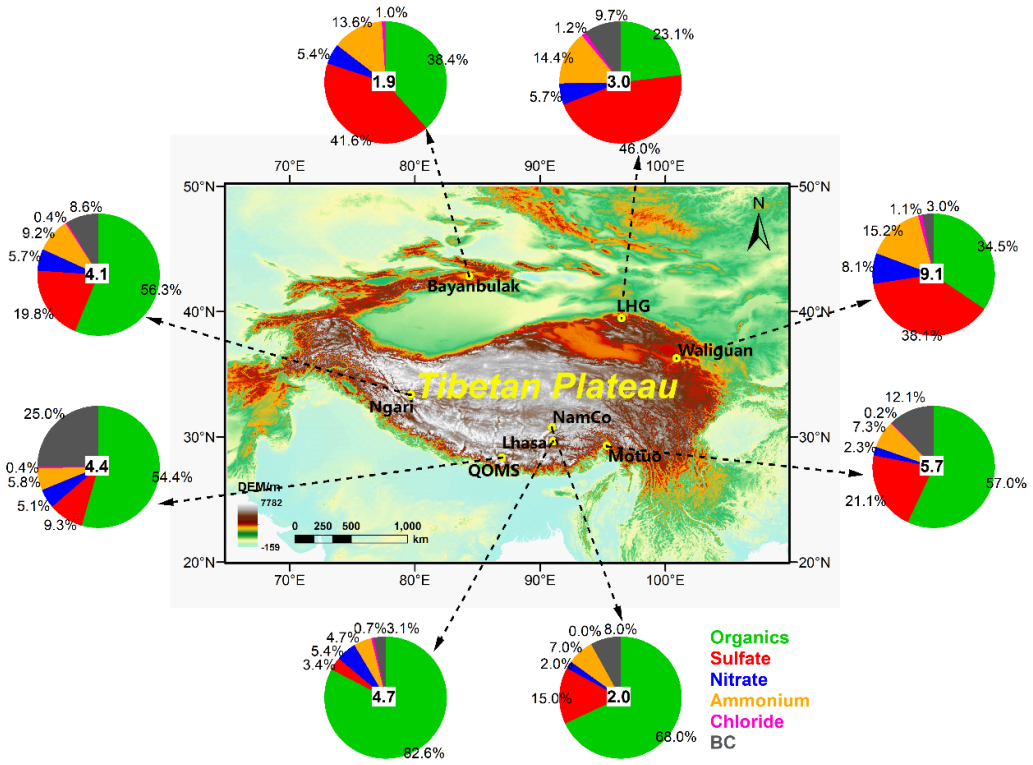

1171

1172 **Figure 2.** Regional distribution of average mass concentrations (values marked in the central of
1173 each pie chart with unit of μg m^{-3}) and chemical compositions (percentage values around each pie
1174 chart) of submicron aerosols (PM_1) during the eight online aerosol field measurements in the Tibetan
1175 Plateau and its surroundings (The geographical base map is created with ArcGIS). The concentration
1176 at each site is presented in ambient condition.

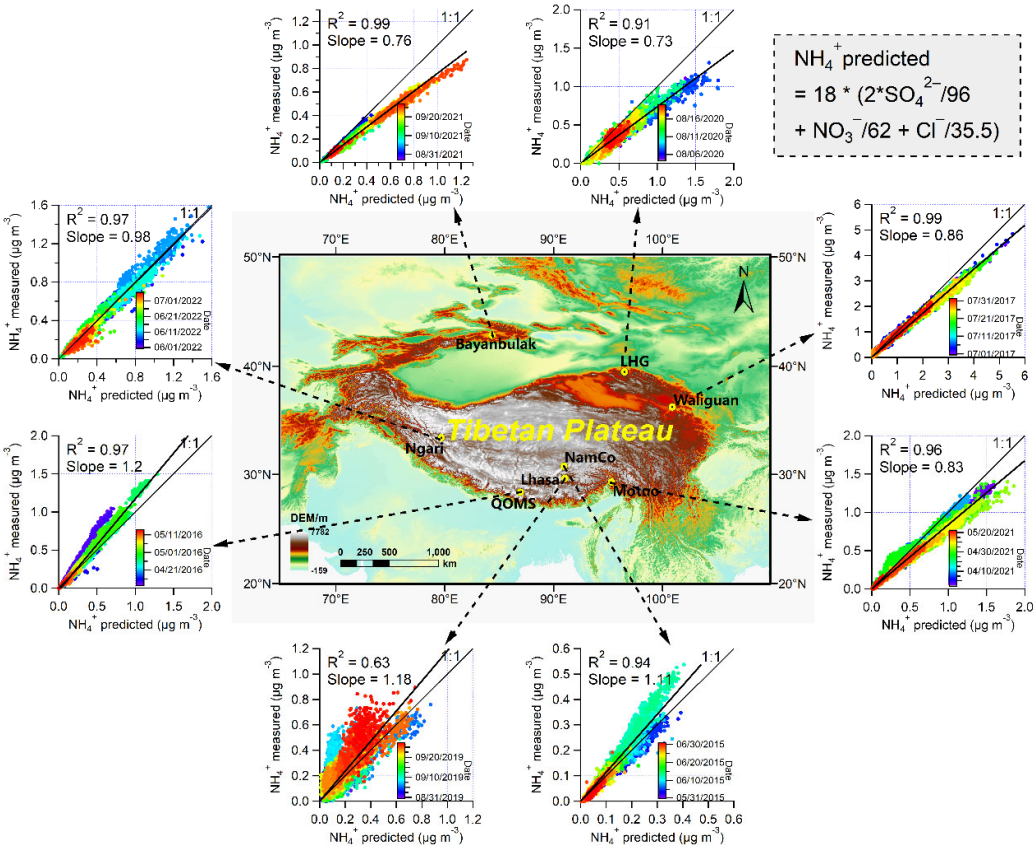

1177

1178 **Figure 3.** Regional difference of bulk acidity of submicron aerosols based on the scatterplot analysis
1179 and linear regression of measured NH_4^+ versus predicted NH_4^+ during the eight aerosol field
1180 measurement campaigns in the Tibetan Plateau and its surroundings (The geographical base map is
1181 created with ArcGIS).

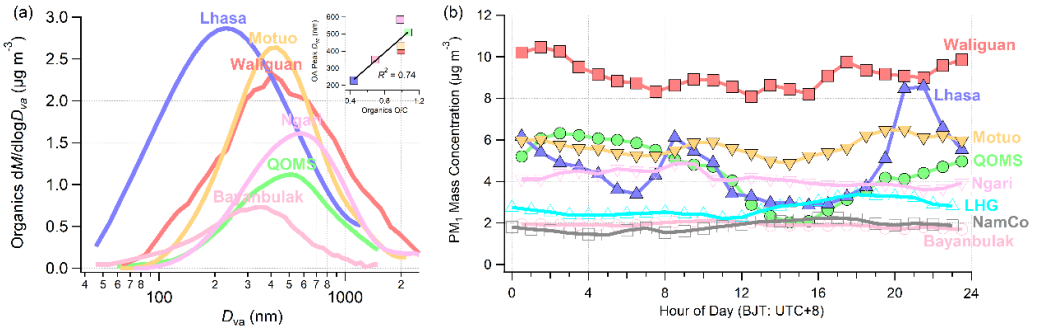

1182

1183 **Figure 4. (a)** Average size distributions of organic mass concentrations during six field
1184 measurement campaigns in the Tibetan Plateau and its surroundings. **(b)** Diurnal variations of total
1185 PM_1 mass concentrations during the eight field measurement campaigns in the Tibetan Plateau and
1186 its surroundings. Insert graph in **(a)** is the scatter plot of peak diameters in their size distributions
1187 versus the average O/C ratio of organics.

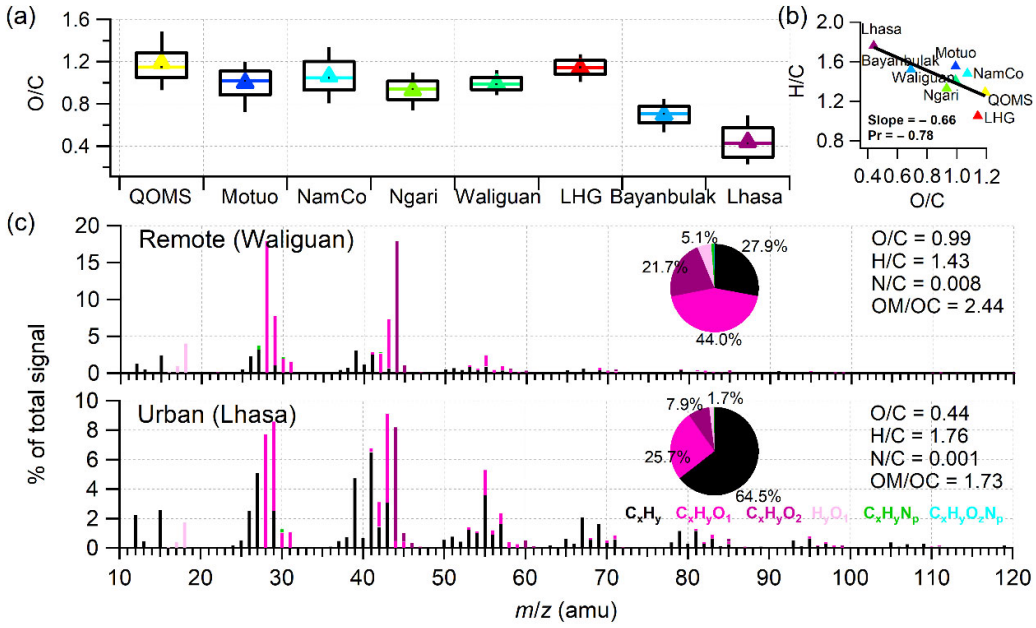

1188

1189 **Figure 5. (a)** Box plots of the average O/C ratios and **(b)** Van Krevelen diagram of H/C versus O/C
1190 among the eight field measurement campaigns in this study. **(c)** The average HRMSs of OA colored
1191 with different ion categories during the Waliguan and Lhasa measurement campaigns. The whiskers
1192 of boxes indicate the 90th and 10th percentiles, the upper and lower boundaries of boxes indicate the
1193 75th and 25th percentiles, the lines in the boxes indicate the median values, the markers indicate the
1194 mean values, and similarly hereinafter.

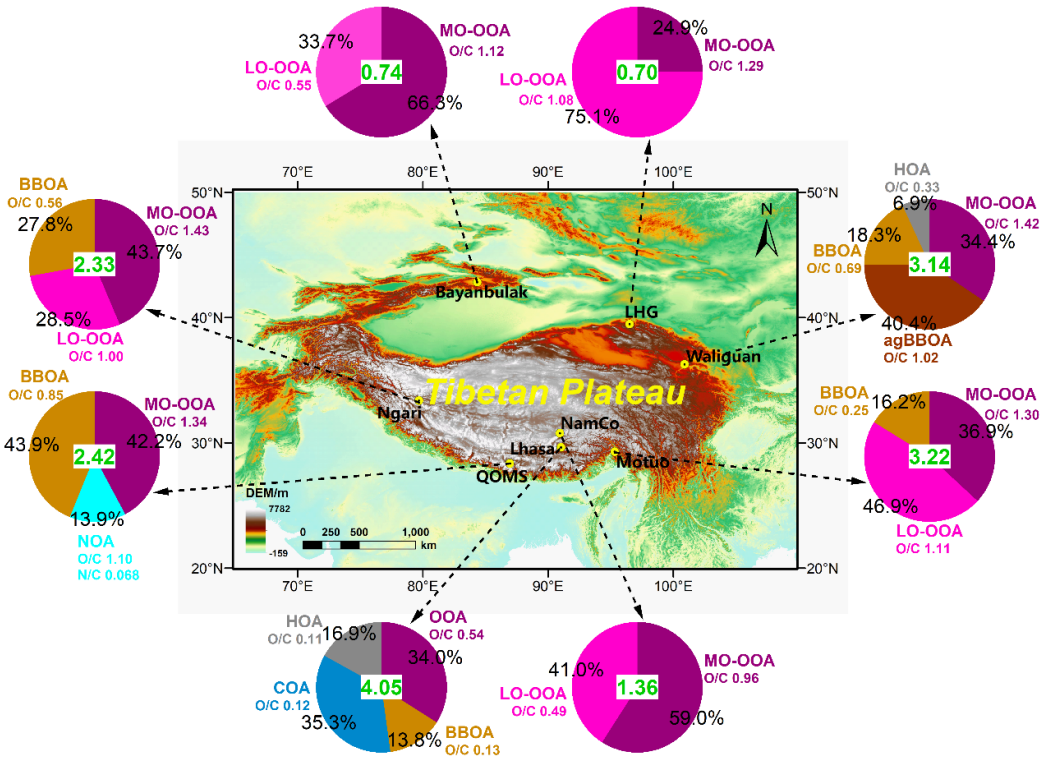

Figure 6. Regional distribution of OA components from PMF source apportionment during the eight online aerosol field measurements in the Tibetan Plateau and its surroundings (The geographical base map is created with ArcGIS). Values marked in the central of each pie chart are average OA mass with unit of μg m^{-3}, while the percentage values around the pie chart are the mass contributions of each OA component. The O/C ratio of each OA component is also marked around each pie chart.

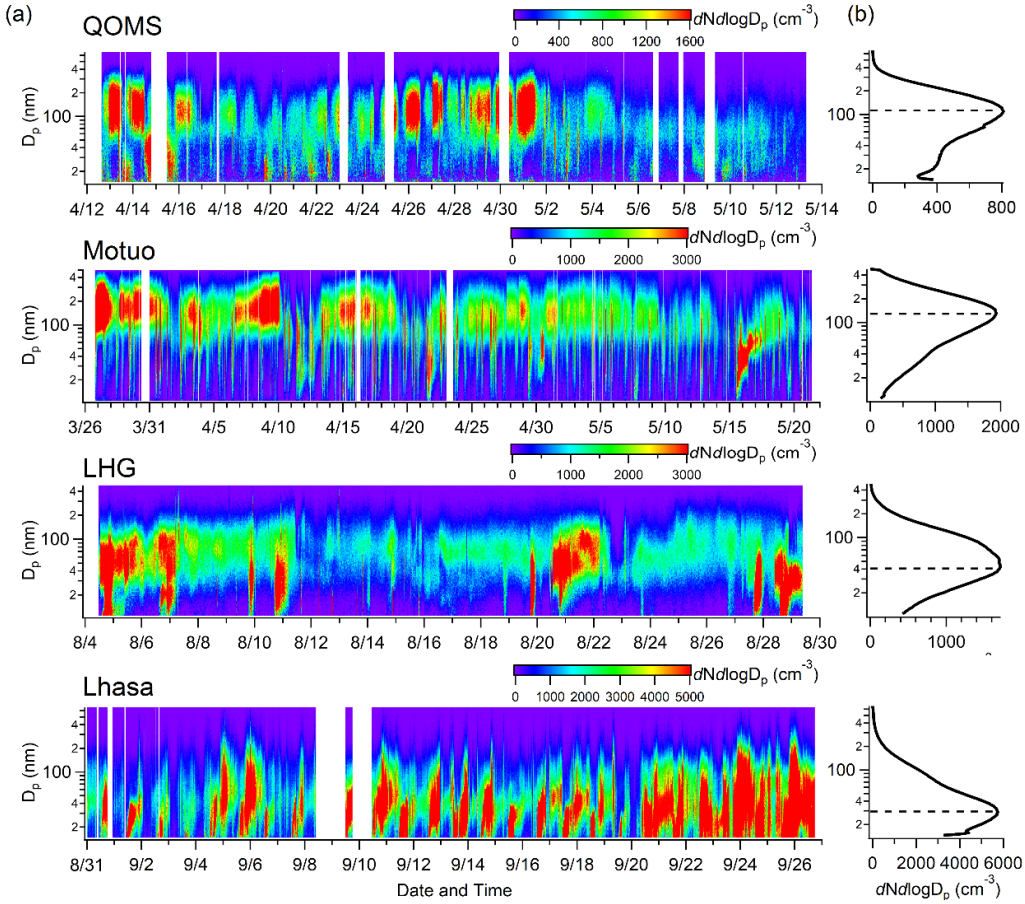

1201

1202 **Figure 7. (a)** Temporal variations of the size distributions of particle number concentrations during
1203 the aerosol field measurement campaigns at QOMS, Motuo, LHG, and Lhasa sites. **(b)** The average
1204 size distribution of particle number concentration during entire measurement period at each site.

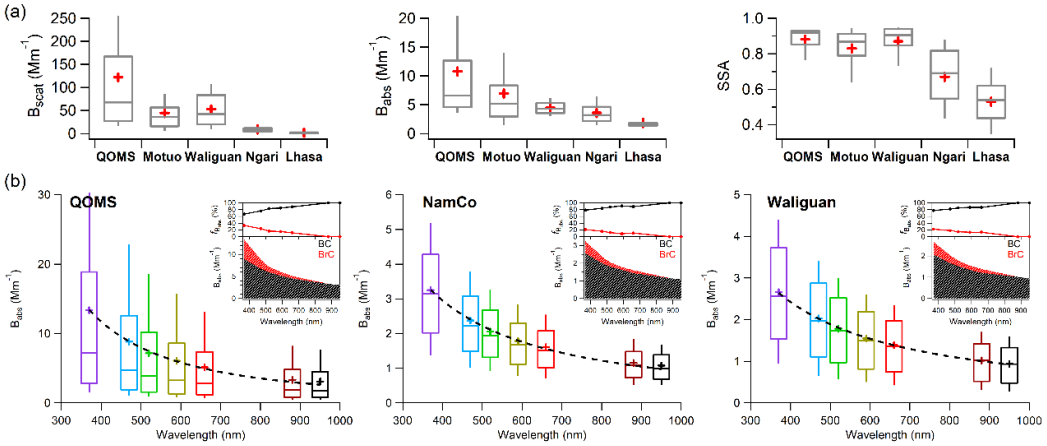

1205

1206 **Figure 8.** Box plots of **(a)** the average particle light scattering coefficient (B_{scat}), light absorption
1207 coefficient (B_{abs}), and single scattering albedo (SSA) during the five aerosol field measurement
1208 campaigns at QOMS, Motuo, Waliguan, Ngari, and Lhasa sites, and **(b)** the particle B_{abs} at seven
1209 wavelengths measured by aethalometers at QOMS, NamCo, and Waliguan sites. The dashed lines
1210 in the boxes in **(b)** show the power-law fit of the average B_{abs} as a function of wavelength. The
1211 inserted plots in **(b)** are the apportioned contributions of BC and BrC to total B_{abs} at different
1212 wavelengths.

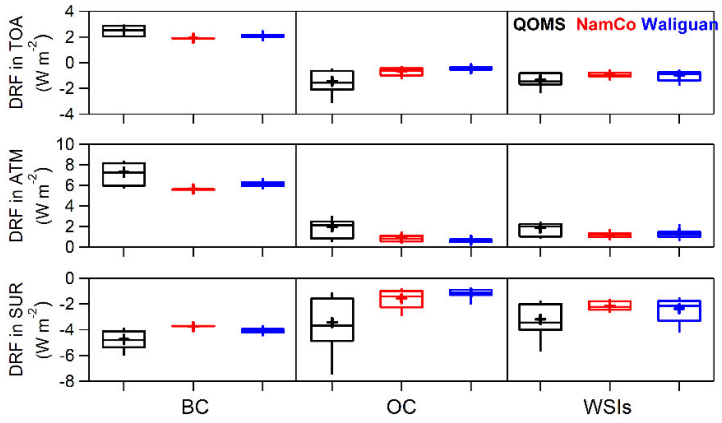

1213

1214 **Figure 9.** Box-plots of the modelled direct radiative forcing (DRF) at the top of the atmosphere
1215 (TOA), the atmosphere (ATM), and the earth's surface (SUR) caused by black carbon (BC), organic
1216 carbon (OC), and water-soluble io ns (WSIs) during the QOMS, NamCo, and Waliguan campaigns.

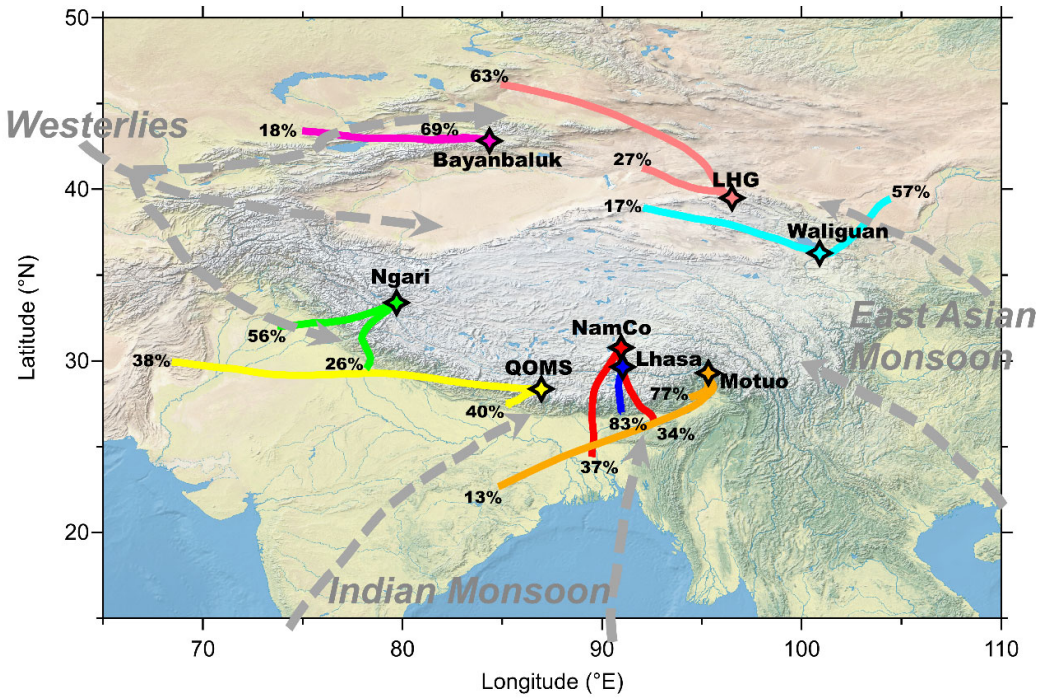

1217

1218 **Figure 10.** Air mass backward trajectory clusters during the eight field campaigns in the Tibetan
1219 Plateau and its surroundings in our study (The geographical base map is created with Igor Pro). Only
1220 major trajectory clusters during each field campaign are displayed with the contributions marked
1221 correspondingly.

Tables

Table 1. Detailed information about the full name and geographic characteristic of observation station, sample period, online instruments, and corresponding references during each aerosol field measurement campaigns over the Tibetan Plateau and its surroundings in this study.

Station	Full Station Name	Lat. (°N)	Long. (°E)	Alt. (m)	Sample Period	Online Instruments						References
						HR-ToF-AMS		SMPS	PAX	Aethalometer	CCN-100	
						MS	PToF					
QOMS	Qomolangma Station for Atmospheric and Environmental Observation and Research, Chinese Academy of Sciences	28.36	86.95	4276	12 April to 12 May 2016	√	√	√	√	√		Zhang et al. (2018) An et al. (2019) Xu et al. (2020) Zhang et al. (2021) Xu et al. (2022)
Motuo	Motuo County, Linzhi City, Tibet Autonomous Region, China	29.30	95.32	1305	26 Mar to 22 May 2021	√	√	√	√		√	This study
NamCo	Nam Co Station for Multisphere Observation and Research, Chinese Academy of Sciences	30.77	90.95	4730	31 May to 1 July 2015	√				√		Xu et al. (2018) Zhang et al. (2021)
Ngari	Ngari Station for Desert Environment Observation and Research, Chinese Academy of Sciences	33.39	79.70	4270	1 Jun to 5 Jul 2022	√	√		√			This study
Waliguan	China Global Atmospheric Watch Baseline Observatory, Mount Waliguan Base	36.28	100.90	3816	1 July to 31 July 2017	√	√		√	√	√	Zhang et al. (2019) Zhang et al. (2020) Xu et al. (2020) Zhang et al. (2021) Xu et al. (2022)
LHG	Qilian Observation and Research Station of Cryosphere and Ecologic Environment, Chinese Academy of Sciences	39.50	96.51	4180	4 August to 29 August 2020	√		√			√	This study
Bayanbulak	Bayanbulak Town, Hejing County, Bayingolin Mongolian Autonomous Prefecture, Xinjiang Uygur Autonomous Region, China	42.83	84.35	2454	29 August to 26 September 2021	√	√					This study
Lhasa	Lhasa City, Tibet Autonomous Region, China	29.65	91.03	3650	31 August to 26 September 2019	√	√	√	√			Zhao et al. (2022)

1227 **Table 2.** Summary of the average values measured with various instruments during the eight aerosol

1228 field measurement campaigns in the TP and its surroundings in this study.

Measurement items	QOMS	Motuo	NamCo	Ngari	Waliguan	LHG	Bayanbulak	Lhasa
HR-ToF-AMS measurements								
PM_1 mass conc. (μg m^{-3})	4.4	5.7	2.0	4.1	9.1	3.0	1.9[a]	4.7
PM_1 chemical compositions (%)								
OA	54.4	57.0	68.0	56.3	34.5	23.1	38.4	82.6
Sulfate	9.3	21.1	15.0	19.8	38.1	46.0	41.6	3.4
Nitrate	5.1	2.3	2.0	5.7	8.1	5.7	5.4	5.4
Ammonium	5.8	7.3	7.0	9.2	15.2	14.4	13.6	4.7
Chloride	0.4	0.2	0	0.4	1.1	1.2	1.0	0.7
BC	25.0	12.1	8.0	8.6	3.0	9.7	N/A	3.1
Peak diameter in mass size distribution (nm)								
OA	510.2	430.5		584.4	405.5		350.8	228.1
SNA	510.2	471.9		634.5	504.7		379.6	250.0
OA components (%)								
MO-OOA	42.2	36.9	59.0	43.7	34.4	24.9	66.3	
LO-OOA		46.9	41.0	28.5		75.1	33.7	
OOA								34.0
BBOA	3.9	16.2		27.8	18.3			13.8
agBBOA					40.4			
NOA	13.9							
HOA					6.9			16.9
COA								35.3
OA elemental ratios								
O/C	1.19	0.99	1.07	0.98	0.99	1.14	0.69	0.44
H/C	1.29	1.55	1.48	1.33	1.41	1.05	1.52	1.76
OM/OC	2.70	2.48	2.57	2.44	2.45	2.62	2.09	1.74
N/C	0.030	0.020	0.016	0.019	0.008	0.011	0.026	0.001
SMPS measurements								
Number conc. (cm^{-3})	709.3	1639.2				1462.0		3994.4
Peak diameter in PNSD (nm)	109.4	131.0				42.9		28.9
PAX measurements								
B_{scat} (Mm^{-1})	121.9	44.9		8.9	36.3			2.1
B_{abs} (Mm^{-1})	10.8	7.0		3.6	4.1			1.9
B_{ext} (Mm^{-1})	132.7	51.9		12.6	40.4			4.0
SSA	0.89	0.83		0.67	0.86			0.52
Aethalometer measurements								
$B_{abs,370}$ (Mm^{-1})	13.40		3.25		2.66			
Absorption Ångström exponent	1.73		1.28		1.12			
$B_{abs,BrC,370}$ (Mm^{-1})	4.42		0.69		0.60			
$B_{abs,BC,370}$ (Mm^{-1})	8.94		2.56		2.06			
$fB_{abs,BrC,370}$ (%)	33.1		21.3		22.4			
$fB_{abs,BC,370}$ (%)	66.9		78.7		77.6			
CCN-100 measurements (cm^{-3})								
CCN number conc. (*SS* 0.2%)		974.0			233.7	120.5		
CCN number conc. (*SS* 0.4%)		1142.6			857.8	340.1		
CCN number conc. (*SS* 0.6%)		1240.1			1138.7	417.8		
CCN number conc. (*SS* 0.8%)		1296.5			1313.1	468.0		
CCN number conc. (*SS* 1.0%)		1337.9			1407.0	504.5		

1229 [a]only non-refractory PM_1 is reported at Bayanbulak due to the absence of BC observation.

Table 3. Summary of the average PM_1 mass concentrations (μg m^{-3}) measured by the Aerodyne AMSs at various high-altitude and remote sites worldwide.

Observation Sites	Latitude (°N)	Longitude (°E)	Altitude (m a.s.l.)	PM_1 mass (μg m^{-3})	References
QOMS, China	28.36	86.95	4276	4.4	This study & Zhang et al. (2018)
Motuo, China	29.30	95.32	1305	5.7	This study
NamCo, China	30.77	90.95	4730	2.0	This study & Xu et al. (2018)
Ngari, China	33.39	79.70	4270	4.1	This study
Waliguan, China	36.28	100.90	3816	9.1	This study & Zhang et al. (2019)
LHG, China	39.50	96.51	4180	3.0	This study
Bayanbulak, China	42.83	84.35	2454	1.9[a]	This study
Lhasa, China	29.65	91.03	3650	4.7	This study & Zhao et al. (2022)
NamCo, China	30.77	90.95	4730	1.06	Wang et al. (2017)
Mt. Yulong, China	27.20	100.20	3410	5.7	Zheng et al. (2017)
Menyuan, China	37.61	101.26	3295	11.4	Du et al. (2015)
Mt. Wuzhi, China	18.84	109.49	958	10.9	Zhu et al. (2016)
Mt. Jungfraujoch, Switzerland	46.55	7.98	3580	0.55	Fröhlich et al. (2015)
Mt. Jungfraujoch, Switzerland	46.55	7.98	3580	2.24	Zhang et al. (2007a)
Mt. Bachelor, USA	43.98	-121.69	2800	15.10	Zhou et al. (2017)
Mt. Whistler, Canada	50.01	-122.95	2182	1.91	Sun et al. (2009)
Mt. Cimone, Italy	44.18	10.70	2165	4.5	Rinaldi et al. (2015)
Puy de Dôme, France	45.77	2.95	1465	5.58	Freney et al. (2011)
Sub-Antarctic Bird Island	-54.00	-38.04		0.46	Schmale et al. (2013)
Mace Head, Ireland	53.30	-9.80		1.53	Zhang et al. (2007a)
Hyytiala, Finland	61.90	24.30		2.04	Zhang et al. (2007a)
Storm Peak, USA	40.50	-106.70		2.11	Zhang et al. (2007a)
Duke Forest, USA	36.00	-79.10		2.82	Zhang et al. (2007a)
Chebogue, Canada	43.80	-66.10		2.91	Zhang et al. (2007a)
Okinawa Island, Japan	26.87	33.51		7.89	Jimenez et al. (2009)
Fukue Island, Japan	32.69	128.84		12.03	Takami et al. (2005)
Cheju Island, Korea	33.51	126.50		10.66	Jimenez et al. (2009)

[a]only non-refractory PM_1 is reported at Bayanbulak due to the absence of BC observation.